Barotropic Growth of Monsoon Depressions

Michael Diaz* and William R. Boos

Department of Earth and Planetary Science, University of California, Berkeley, USA

Although monsoon depressions are a principal synoptic-scale element of the South Asian monsoon, producing extreme rainfall over India and surrounding regions, there exists no widely accepted mechanism explaining their occurrence. This study presents a hierarchy of numerical experiments aimed at finding such an explanation. Using a perturbation-basic state decomposition, we derive an anelastic system of equations that can represent disturbances growing in the complex, three-dimensional monsoon basic state. We find that modal solutions to these equations linearized about this basic state can explain many features of observed monsoon depressions, including their warm-over-cold core structure, westward propagation, and lower-tropospheric wind maximum. For the zonally symmetric case, these modes are barotropically unstable, drawing energy from the meridional shear of the monsoon trough. For the zonally varying basic state, modal solutions still derive energy from barotropic conversion, but fail to achieve positive net growth rates when dissipative processes are included. For the non-linear equation set, these modes can be excited by a heating impulse, and their energy then remains roughly constant over several days as barotropic energy transfers oppose dissipative losses. Our results support the idea that the general concept of barotropic instability can explain the structure, propagation, and geographic distribution of monsoon depressions, but not their rapid growth rates. We speculate that condensational heating coupled to these waves is needed to obtain a positive growth rate.

Key Words: monsoon depression; barotropic instability; monsoon low pressure system; Indian monsoon; idealized numerical modeling

Received . . .

1. Introduction

At first glance, Indian monsoon depressions appear to have much in common with tropical cyclones: they typically form over warm water, have a deep, cyclonic circulation, and produce copious rainfall. Yet in many ways they are quite different. Their circulation rarely achieves the intensity, symmetry, and small scale of the core of a mature tropical cyclone, instead remaining broad and weak with more loosely organized precipitation. Additionally, in contrast with the deep warm core of tropical cyclones, which extends through the full depth of the troposphere, the core of a monsoon depression transitions from warm at upper levels to cold at lower levels. They can also form and strengthen over land, a feat rare for tropical cyclones (Arndt et al. 2009). Furthermore, being embedded within the larger-scale South Asian monsoon, monsoon depressions are often subjected to strong vertical wind shear, a well-known detriment to tropical cyclogenesis.

Based on these dissimilarities, one could reasonably argue that the mechanism by which monsoon depressions form and intensify differs from that of tropical cyclones. It has long been recognized that the presence of horizontal and vertical wind shear associated with the large-scale monsoon circulation may lead to the growth of monsoon depressions through a dynamic instability (e.g. Rao 1971; Krishnamurti et al. 1976; Sikka 1977). However, there is little consensus as to how this mechanism would operate. Some have suggested that the large-scale monsoon flow is baroclinically unstable (Mishra and Salvekar 1980; Saha and Chang 1983; Salvekar and Mishra 1985; Salvekar et al. 1986). However, Moorthi and Arakawa (1985) argued that the easterly vertical shear in this region is too weak to support baroclinic instability in the traditional sense. Instead, they proposed that monsoon depressions arise through moist baroclinic instability, a process that requires condensational heating from precipitation as an additional energy source (see also Krishnakumar et al. 1992; Kasture et al. 1993). Nevertheless, this explanation is still problematic, because existing theories for baroclinic instability, whether dry or moist, require that the disturbance tilts upshear with height (Cohen and Boos 2016). Monsoon depressions by contrast generally exhibit either no tilt or a slightly downshear tilt (Keshavamurty 1972; Hunt et al. 2016a; Cohen and Boos 2016). Some evidence even suggests that vertical shear hinders their formation (Ditchek et al. 2016).

Even if the vertical shear of the large-scale monsoon flow is not unstable baroclinically, its horizontal shear could be unstable barotropically. Yet many of the studies that have explored this possibility have cast doubt on its relevance to monsoon depressions. For example, a linear instability analysis by Shukla (1977) found that the most unstable normal mode of a basic state

representative of the monsoon region has a westward phase speed of $15\,\mathrm{m\,s^{-1}}$ and maximum amplitude in the upper troposphere, both inconsistent with observed monsoon depressions, whose phase speed is typically westward near $3\,\mathrm{m\,s^{-1}}$ and whose strongest amplitude is in the lower troposphere. This discrepancy led Shukla (1977) to conclude that barotropic instability cannot explain the occurence of monsoon depressions. Additionally, most idealized modeling studies that invoke moist baroclinic instability as a dominant growth mechanism find that barotropic energy conversion is small or negative (Krishnakumar et al. 1992; Kasture et al. 1993). Some observational analyses of the energetics of individual monsoon depressions seem to support these results. Krishnamurti et al. (2013) found that, for a sample of four monsoon depressions during the year 1996, energy was transferred from the perturbation flow to the zonal-mean flow, a direction indicative of decay through barotropic conversion. Rajamani (1985) and Rajamani and Sikdar (1989) came to similar conclusions for monsoon depressions observed during July 1963 and August 1979, respectively.

On the other hand, some studies have found evidence to support barotropic instability. Subrahmanyam et al. (1981) and Nitta and Masuda (1981) found barotropically unstable normal modes in the mid-tropospheric flow. However, in both of these studies, the phase velocity of these modes is eastward, opposite that of typical monsoon depressions. Goswami et al. (1980) found barotropic instability in the mid-tropospheric flow over western India, but determined the flow over eastern India and southeast Asia, where monsoon depressions generally form, to be barotropically stable. Noting the conflicting results of previous studies, all of which used normal-mode instability theory, Lindzen et al. (1983) used a pulse asymptotics approach and found instabilities in the 500 hPa flow with a wavelength of 2600 km and westward phase speed of $1.5\,\mathrm{m\,s^{-1}}$, both in good agreement with typical values. Barotropic instability also has some observational support. Ditchek et al. (2016) identified low-level absolute vorticity, of which the horizontal shear of the monsoon trough is a large component, to be an important variable in their regression model of genesis frequency. Moreover, several case studies found barotropic conversion to be an energy source for monsoon depressions, though it is generally secondary to the energy source from cumulus convection (Krishnamurti et al. 1976; Nitta and Masuda 1981; Nagar et al. 2009). Recently, Mishra (2018) determined that the monsoon trough becomes increasingly barotropically unstable preceding monsoon depression formation.

Regardless of how relevant the background shear may be, most studies conclude that moist convection plays an essential role in monsoon depression growth. In a modeling study of an observed monsoon depression, Krishnamurti et al. (1976) found that its primary energy source was diabatic heating by cumulus convection. Additionally, three of the four variables used in the genesis index of Ditchek et al. (2016) relate to humidity or to how favorable the environment is for moist convection. Unfortunately, incorporating this aspect of monsoon depression dynamics into the framework of linear instability theory has proven difficult. Some studies have argued that conditional instability of the second kind (CISK) may apply to monsoon depressions. Shukla (1978) considered CISK but found maximum growth rates at the smallest scale and significant discrepancies with observed monsoon depressions (their Fig. 6). Since the time of that and related studies, the CISK mechanism itself has been discredited (for an overview, see Montgomery and Smith 2014) and thus any explanation relying on CISK should be treated with skepticism. More recently, Adames and Ming (2018a) explain monsoon depression growth through a moisture-vortex instability that has diabatic heating from convection as a primary energy source; they note, however, that this instability requires meridional advection of temperature to be weak while meridional advection of moisture is strong, in disagreement with observations presented in their previous work (Adames and Ming 2018b).

Although it is possible that one of the aforementioned growth processes generates monsoon depressions *in situ*, some studies have argued that the initial disturbance might propagate into the monsoon domain from remote regions. For example, Krishnamurti et al. (1977) proposed that monsoon depressions in the Bay of Bengal may originate from energy dispersed from disturbances in the western Pacific (i.e. a westward group velocity allows western Pacific disturbances to cause the formation of Bay of Bengal depressions). Others have suggested that monsoon depressions originate directly from individual western Pacific low pressure systems that propagate westward into the Bay of Bengal (Saha et al. (1981); Chen and Weng (1999)). Nevertheless, even if these mechanisms are correct, they do not explain the localization and rapid growth of disturbances in the vicinity of the Bay of Bengal.

The preceding discussion demonstrates that there is still no widely agreed-upon explanation for how monsoon depressions form. Why do past studies come to such different conclusions? One source of discrepancy may lie in the various ways in which previous idealized modeling experiments have simplified the equations governing atmospheric flow. Though a few consider basic states with both horizontal and vertical shear, many neglect one or the other. For instance, Lindzen et al. (1983) performed their pulse asymptotics analysis of barotropic instability using simple piecewise-linear approximations of the monthly mean flow at either 200 hPa or 500 hPa and did not examine the lower troposphere or the effects of vertical shear. Additionally, almost all previous studies are based on quasi-geostrophic assumptions and resort to linearizing their governing equations. Both of these simplifications are questionable for a strong vortex at low latitudes. Furthermore, almost all of these studies use a zonally homogeneous basic state. Such a simplification implies that the scale of the disturbance is much smaller than that of the basic state. Given that the wavelength of monsoon depressions is similar to the length of the monsoon trough, which is commonly treated as a major feature of the basic state, this assumption may be violated. Past results may also differ because of sensitivity to the choice of basic state. The large-scale flow in the vicinity of the Bay of Bengal can vary substantially from day to day and it is not obvious how to specify a basic state that favors monsoon depressions. Finally, the treatment of convection in previous studies has been highly simplified and may be unrealistic.

The goal of this study is to work toward an explanation of how monsoon depressions form using a series of idealized numerical modeling experiments of increasing complexity. As with many previous studies, our starting hypothesis is that the background flow of the large-scale monsoon is important for their growth and that they can be modeled as perturbations growing on this flow. To improve upon previous studies, we will derive an equation set that minimizes simplifying assumptions regarding the structure of these perturbations and allows for three-dimensional variations in the basic state flow. We will also more carefully construct a basic state to represent the environment in which monsoon depressions grow using a modern reanalysis product. Although we neglect latent heating from convection, which many studies have noted to be important, our results suggest that many aspects of monsoon depressions can be explained without it. In future work, we plan to address its role by extending our modeling framework to include moist convection.

This study is outlined as follows: Section 2 presents a derivation of our governing equation set and a description of how we construct the basic state, Secs. 3 and 4 present a linear instability

analysis of the zonally symmetric basic state (Exp. A) and zonally varying basic state (Exp. B), Sec. 5 presents an initial value problem using the non-linear equation set (Exp. C), and Sec. 6 summarizes our results.

2. Methods

Here we derive a closed equation set that describes the time evolution of a perturbation on a three-dimensional time-independent basic state. Although the derivation is for the non-linear case, we will linearize it in subsequent sections for some of our experiments.

2.1. *Model Equations*

The equations of motion for a dry, rotating atmosphere in Cartesian height coordinates can be expressed as

$$\frac{\partial \mathbf{u}}{\partial t} + \mathbf{u}\cdot\nabla\mathbf{u} = -\frac{1}{\rho}\nabla p - g\hat{\mathbf{k}} - f\hat{\mathbf{k}}\times\mathbf{v} + \mathbf{S} \tag{1a}$$

$$\frac{\partial \theta}{\partial t} + \mathbf{u}\cdot\nabla\theta = S_\theta \tag{1b}$$

$$\frac{\partial \rho}{\partial t} + \nabla\cdot(\rho\mathbf{u}) = 0 \tag{1c}$$

$$\theta = T\left(\frac{p_r}{p}\right)^{\frac{R}{c_p}} \tag{1d}$$

$$p = \rho R T \tag{1e}$$

where $\mathbf{u} = \langle u, v, w\rangle$, $\mathbf{v} = \langle u, v\rangle$, $\mathbf{S}$ is a momentum source, S_θ is a heat source, f is the Coriolis parameter, which varies as a function of latitude, and all other symbols have their usual meaning.

We first partition the thermodynamic fields into a vertically varying base state, which is in hydrostatic balance, and a perturbation,

$$\rho = \rho_0(z) + \tilde{\rho}(\mathbf{r}, t) \tag{2a}$$

$$p = p_0(z) + \tilde{p}(\mathbf{r}, t) \tag{2b}$$

$$\theta = \theta_0(z) + \tilde{\theta}(\mathbf{r}, t) \tag{2c}$$

where $\mathbf{r} \equiv \langle x, y, z\rangle$. We then make the anelastic approximations, assuming that the base state values are much larger than the perturbations and replacing density by its base state value except where it multiplies gravity. From these assumptions, we can derive the following equations:

$$\frac{\partial \mathbf{u}}{\partial t} + \mathbf{u}\cdot\nabla\mathbf{u} = -\nabla\tilde{\phi} + g\frac{\tilde{\theta}}{\theta_0}\hat{\mathbf{k}} - f\hat{\mathbf{k}}\times\mathbf{v} + \mathbf{S} \tag{3a}$$

$$\frac{\partial \tilde{\theta}}{\partial t} + \mathbf{u}\cdot\nabla\tilde{\theta} + w\frac{d\theta_0}{dz} = S_\theta \tag{3b}$$

$$\nabla\cdot(\rho_0\mathbf{u}) = 0 \tag{3c}$$

where $\tilde{\phi} \equiv \frac{\tilde{p}}{\rho_0}$. A full derivation of the anelastic equations of motion is given in Sec. 2 of Bannon (1995). For our purposes, the anelastic equation set has several advantages. First, it filters out acoustic waves, which require prohibitively small time steps for numerical integration. Second, it eliminates Eqs. 1d and 1e, whose partitioning into a basic state and perturbation is complicated and difficult to linearize. Finally, because it remains non-hydrostatic, it can be extended to high-resolution convection-resolving simulations in future work.

Each of the fields can be partitioned into a time-independent basic state and a time-dependent perturbation. Let

$$\mathbf{u} = \bar{\mathbf{U}}(\mathbf{r}) + \mathbf{u}'(\mathbf{r}, t) \tag{4a}$$

$$\tilde{\phi} = \bar{\Phi}(\mathbf{r}) + \phi'(\mathbf{r}, t) \tag{4b}$$

$$\tilde{\theta} = \bar{\theta}(\mathbf{r}) + \theta'(\mathbf{r}, t) \tag{4c}$$

$$\mathbf{S} = \bar{\mathbf{S}}(\mathbf{r}) + \mathbf{s}'(\mathbf{r}, t) \tag{4d}$$

$$S_\theta = \bar{S}_\theta(\mathbf{r}) + s'_\theta(\mathbf{r}, t) \tag{4e}$$

where terms with overbars represent the basic state and terms with primes the perturbation. Note the distinction between the vertically varying *base* state used in the anelastic approximation (Eq. 2) and the three-dimensionally varying *basic* state defined in Eq. 4. Substituting Eq. 4 into Eqs. 3a, 3b, and 3c yields

$$\frac{\partial \mathbf{u}'}{\partial t} + (\bar{\mathbf{U}} + \mathbf{u}')\cdot\nabla(\bar{\mathbf{U}} + \mathbf{u}') =$$
$$-\nabla(\bar{\Phi} + \phi') + g\left(\frac{\bar{\theta} + \theta'}{\theta_0}\right)\hat{\mathbf{k}} - f\hat{\mathbf{k}}\times(\bar{\mathbf{V}} + \mathbf{v}') + \bar{\mathbf{S}} + \mathbf{s}' \tag{5a}$$

$$\frac{\partial \theta'}{\partial t} + (\bar{\mathbf{U}} + \mathbf{u}')\cdot\nabla(\bar{\theta} + \theta') + (\bar{W} + w')\frac{d\theta_0}{dz} = \bar{S}_\theta + s'_\theta \tag{5b}$$

$$\nabla\cdot(\rho_0(\bar{\mathbf{U}} + \mathbf{u}')) = 0 \tag{5c}$$

where $\bar{\mathbf{V}}$ and $\mathbf{v}'$ are the horizontal components of $\bar{\mathbf{U}}$ and $\mathbf{u}'$, respectively.

In order for the basic state to remain stationary, it must be a time-independent solution to Eqs. 3a, 3b, and 3c. This constraint implies that

$$\bar{\mathbf{U}}\cdot\nabla\bar{\mathbf{U}} = -\nabla\bar{\Phi} + g\frac{\bar{\theta}}{\theta_0}\hat{\mathbf{k}} - f\hat{\mathbf{k}}\times\bar{\mathbf{V}} + \bar{\mathbf{S}} \tag{6a}$$

$$\bar{\mathbf{U}}\cdot\nabla\bar{\theta} + \bar{W}\frac{d\theta_0}{dz} = \bar{S}_\theta \tag{6b}$$

$$\nabla\cdot(\rho_0\bar{\mathbf{U}}) = 0 \tag{6c}$$

Equations 6a, 6b, and 6c are the governing equations for the basic state. In this context, $\bar{\mathbf{S}}$ and $\bar{S}_\theta$ are the momentum and heat sources necessary to keep the basic state time-independent. Subtracting Eqs. 6a, 6b, and 6c from Eqs. 5a, 5b, and 5c, respectively, and rearranging yields the following:

$$\frac{\partial \mathbf{u}'}{\partial t} = -(\bar{\mathbf{U}} + \mathbf{u}')\cdot\nabla\mathbf{u}' - \mathbf{u}'\cdot\nabla\bar{\mathbf{U}} - \nabla\phi' + g\frac{\theta'}{\theta_0}\hat{\mathbf{k}} - f\hat{\mathbf{k}}\times\mathbf{v}' + \mathbf{s}' \tag{7a}$$

$$\frac{\partial \theta'}{\partial t} = -(\bar{\mathbf{U}} + \mathbf{u}')\cdot\nabla\theta' - \mathbf{u}'\cdot\nabla\bar{\theta} - w'\frac{d\theta_0}{dz} + s'_\theta \tag{7b}$$

$$\nabla\cdot(\rho_0\mathbf{u}') = 0 \tag{7c}$$

Finally, we use Eqs. 7a and 7c to derive a diagnostic equation for ϕ'. Multiplying Eq. 7a by ρ_0, taking its divergence, and using Eq. 7c to remove the time derivative yields

$$\frac{\partial^2\phi'}{\partial x^2} + \frac{\partial^2\phi'}{\partial y^2} + \frac{\partial}{\partial z}\left(\rho_0\frac{\partial\phi'}{\partial z}\right) = \nabla\cdot(\rho_0 G\{\mathbf{u}'\}) \tag{8}$$

where the operator G includes all of the terms on the right-hand side of Eq. 7a except for those involving pressure gradients. This is a version of the anelastic pressure equation. Equations 7a, 7b, and 8 form a set of five equations and five unknowns (u', v', w', θ', ϕ') that we can solve using standard numerical methods. The terms $\mathbf{s}'$ and s_θ will be either specified or expressed in terms of the other variables.

2.2. *Numerical Methods*

To solve our equation set (i.e. Eqs. 7a, 7b, and 8), the required field are discretized onto a staggered C-grid (Arakawa and Lamb 1977), where the velocity components occupy the faces of a control volume and all scalars occupy the center of the control volume. To solve numerically, all advection terms in Eqs. 7a and 7b are expressed in flux form, which has better mass-conserving properties compared to advective form. Advection of a generic variable q can be expressed as

$$\mathbf{u}\cdot\nabla q = \frac{1}{\rho_0}[\nabla\cdot(\rho_0 q\mathbf{u}) - q\nabla\cdot(\rho_0\mathbf{u})] \tag{9}$$

Using Eq. 3c to eliminate the second term on the right-hand side of Eq. 9 yields

$$\mathbf{u} \cdot \nabla q = \frac{\partial (qu)}{\partial x} + \frac{\partial (qv)}{\partial y} + \frac{1}{\rho_0} \frac{\partial (\rho_0 qw)}{\partial z} \tag{10}$$

The horizontal and vertical spatial derivatives are evaluated using an upwind-biased fifth-order and third-order accurate approximation, respectively. Time derivaties use a third-order accurate Runge-Kutta scheme. Details of these methods are given in Wicker and Skamarock (2002).

To solve Eq. 8, we adapt a version of the projection method originally proposed by Chorin (1968). In the first step, an intermediate velocity field $\mathbf{u}^*$ is calculated at time n by integrating all of the terms in Eq. 7a except for the pressure gradient term for one time step Δt, yielding

$$\mathbf{u}^* = \mathbf{u}'_\mathbf{n} + G\{\mathbf{u}'_\mathbf{n}\}\Delta t \tag{11}$$

Equation 8 is then solved for ϕ' using $\mathbf{u}^*$ in place of $G\{\mathbf{u}'\}$. This solution requires inverting the three-dimensional Laplacian operator. To do this efficiently, we use a method based on Fast Fourier transforms in the horizontal direction and Gaussian elimination in the vertical. The lateral boundary condition is periodic and the upper and lower are zero pressure gradient. Since the prognostic variables are damped to zero at the lateral boundaries, as described below, they are effectively zero-gradient also. The final velocity is then calculated by

$$\mathbf{u}'_{\mathbf{n+1}} = \mathbf{u}^* + \nabla \phi' \Delta t \tag{12}$$

2.3. *Boundary Conditions*

Near the lateral boundaries, perturbations are damped by adding a source term to the left-hand side of Eqs. 7a and 7b which has the form

$$s_{q^{lb}} = -Aq' \tag{13}$$

where q is substituted with u, v, w, or θ, depending on the context, and A is a damping coefficient. This coefficient is defined as

$$A = \frac{1}{2}\left[1 - \cos\left(\frac{b\pi}{B}\right)\right] \tag{14}$$

where B is the width of the damping region and b varies linearly from a value of zero at the interiormost edge of the damping region to a value of B at its exteriormost edge. A damping layer is also placed near the upper boundary. Its primary purpose is to dissipate stratospheric gravity waves that would otherwise by reflected back downward by the rigid upper boundary. It is described by

$$s_{q^{ub}} = -0.05Aq' \tag{15}$$

and its width is set to five grid points in most of our experiments. At the upper and lower boundaries, the vertical velocity and pressure gradient are set to zero.

2.4. *Basic State*

To be relevant to monsoon depressions, the basic state flow (i.e. $\bar{U}$, $\bar{V}$, $\bar{W}$, and $\bar{\theta}$) must represent the environment in which these storms typically form and grow. One approach would be to use a time mean of the atmospheric state over South Asia during the summer monsoon. However, because the flow over this region can vary substantially from day to day, this time mean would combine many different flow configurations and potentially yield an overly-smoothed basic state. If environmental wind shear is important for monsoon depression growth, such an outcome would be unsatisfactory. Since many of the atmospheric states occurring in this region may not even support monsoon depression growth, a better approach would be to use an average from environments in which monsoon depressions actually formed. However, this alternative creates a different problem: such an average may be overly influenced by the monsoon depressions themselves. Keeping these issues in mind, our procedure for constructing a basic state attempts to satisfy the competing goals of averaging out small-scale noise, retaining the strong horizontal shear of the monsoon trough and the strong vertical shear of the zonal wind, and minimizing the impact of monsoon depressions on the average.

To find environments that favor monsoon depressions, we use the monsoon depression track dataset of Hurley and Boos (2015). We select all monsoon depressions that formed in the rectangle bounded by 17°N, 23°N, 85°E, and 100°E during June through September from 1979 to 2012. These criteria lead to 64 cases. Each case is then paired with the corresponding fields from the ERA-Interim reanalysis (Dee et al. 2011), which is available every six hours. We then construct a basic state for each case using a short-term average. Attempting to exclude the monsoon depressions, we first tried averaging periods preceding the genesis time identified by the tracking algorithm. However, new monsoon depressions are preceded by older ones with enough frequency to leave an imprint of the previous monsoon depression in the time-mean fields. We thus decided on averaging the 36 hours following and including the genesis time, which amounts to six individual times per case. During this period, the initial disturbance found by the tracking algorithm tended to be weak enough not to leave a clearly discernable vortex in the time-mean fields. Furthermore, computing averages in standard latitude-longitude coordinates rather than storm-relative coordinates led to a greater smoothing of any vortices that existed at genesis.

Even with these constraints, the basic states still vary substantially. Some of this variability results from the monsoon trough moving north and south. Another problem is that the starting point identified by the algorithm may be well before the time period of most significant growth. To further avoid averaging dissimilar basic states, we perform an Empirical Orthogonal Function (EOF) analysis to stratify the genesis states. For the set of 64 basic states derived above, we compute an EOF of the the zonal wind within a volume bounded by 13.7°N, 29.1°N, 72.4°E, 102.7°E, 550 hPa, and 875 hPa. The first EOF, which explains 35.8% of the variance, corresponds to the monsoon trough moving north and south or strengthening and weakening. We then average over times that project strongly onto this EOF, which corresponds to states with well-developed easterly flow to the north of the monsoon westerlies, a pattern indicative of a well-defined monsoon trough. This restriction reduces our total number of genesis cases to 31 and ultimately leads to averaging 186 individual times into our basic state. These times are well distributed throughout the diurnal cycle with a minimum of 22.0% for 12 UTC and a maximum of 28.0% for 00 UTC. The result is shown in Fig. 1. Consistent with our aim, it has a well-developed monsoon trough and much of the small-scale noise has been averaged out. By contrast, the basic state derived from the other phase of the EOF does not have a well-defined monsoon trough (not shown) and does not yield growing disturbances for any of our experiments. Hence, we will not include it in this study.

2.5. *Energetics Equation*

To gain physical insight into how perturbations interact with the basic state, it is useful to derive an equation for the kinetic energy of the horizontal perturbation wind. Taking the dot product of the

horizontal velocity vector $\mathbf{v}'$ with Eq. 7a yields

$$\frac{\partial K_p}{\partial t} + (\bar{\mathbf{U}} + \mathbf{u}') \cdot \nabla K_p + u'v'\frac{\partial \bar{U}}{\partial y} + u'v'\frac{\partial \bar{V}}{\partial x} + u'^2\frac{\partial \bar{U}}{\partial x} + v'^2\frac{\partial \bar{V}}{\partial y} + u'w'\frac{\partial \bar{U}}{\partial z} + v'w'\frac{\partial \bar{V}}{\partial z} = -\mathbf{v}' \cdot (\frac{\partial \phi'}{\partial x}\hat{\mathbf{i}} + \frac{\partial \phi'}{\partial y}\hat{\mathbf{j}}) + \mathbf{v}' \cdot (s'_u\hat{\mathbf{i}} + s'_v\hat{\mathbf{j}}) \quad (16)$$

where $K_p \equiv \frac{u'^2+v'^2}{2}$ is the perturbation kinetic energy. The first two terms on the left-hand side are the local rate of change of K_p and the advection of K_p by the mean and perturbation flow. The next six terms are exchanges between the kinetic energy of the mean flow and the perturbation, a process commonly referred to as barotropic conversion. The first term on the right-hand side of the equation is the work done by the pressure gradient force. As shown by Orlanski and Chang (1993), this term can be decomposed into the baroclinic term, which is associated with warm air rising and cold air sinking, and a boundary pressure work term. Since the standard baroclinic term is not strictly valid on a limited domain, we will use the pressure work term directly. The final term in Eq. 16 is frictional dissipation.

3. Zonally Homogeneous Basic State (Exp. A)

In our first set of experiments, we find normal mode solutions to our equation set linearized about the basic state we have constructed from reanalysis data. In this section, we restrict our analysis to zonally homogeneous basic states (we will call this Exp. A). Solutions using zonally inhomogeneous basic states are derived in Sec. 4 (Exp. B). Details about the specific model settings used in this and subsequent sections are listed in Tab. 1.

3.1. *Experimental Design*

This experiment requires a few simplifications to the original equation set. Equations 7a and 7b are linearized by eliminating all of the time-dependent quadratic terms. To make the basic state zonally homogeneous, we use meridional cross sections at select longitudes, i.e. $\mathbf{r} = \langle x_0, y, z\rangle$ for $\bar{U}(\mathbf{r})$ and $\bar{\theta}(\mathbf{r})$ with x_0 being a constant. Additionally, $\bar{V}$ and $\bar{W}$ are set to zero. With these changes, Eqs. 7a and 7b become

$$\frac{\partial \mathbf{u}'}{\partial t} = -\bar{U}\frac{\partial \mathbf{u}'}{\partial x} - v'\frac{\partial \bar{U}}{\partial y} - w'\frac{\partial \bar{U}}{\partial z} - \nabla\phi' + g\frac{\theta'}{\theta_0}\hat{\mathbf{k}} - f\hat{\mathbf{k}} \times \mathbf{v}' + \mathbf{s}' \quad (17a)$$

$$\frac{\partial \theta'}{\partial t} = -\bar{U}\frac{\partial \theta'}{\partial x} - v'\frac{\partial \bar{\theta}}{\partial y} - w'\frac{\partial \bar{\theta}}{\partial z} - w'\frac{d\theta_0}{dz} + s'_\theta \quad (17b)$$

To represent dissipative processes, we add two physical parameterizations to Eq. 17

$$\mathbf{s}' = -s_0(z)(u'\hat{\mathbf{i}} + v'\hat{\mathbf{j}}) + \alpha_y[\frac{\Delta x^6}{\Delta t}]\frac{\partial^6 \mathbf{u}'}{\partial y^6} + \alpha_z[\frac{\Delta z^6}{\Delta t}]\frac{\partial^6 \mathbf{u}'}{\partial z^6} \quad (18a)$$

$$\mathbf{s}'_\theta = \alpha_y[\frac{\Delta x^6}{\Delta t}]\frac{\partial^6 \theta'}{\partial y^6} + \alpha_z[\frac{\Delta z^6}{\Delta t}]\frac{\partial^6 \theta'}{\partial z^6} \quad (18b)$$

where s_0 and α are constants whose values are given in Tab. 1 and s_0 is zero everywhere except at the lowest model level, which is located 250 m above the surface. The first term on the right hand side of Eq. 18a represents low-level friction. Including friction is essential because it has been found to stabilize a variety of atmospheric instability phenomena (e.g. Hall and Sardeshmukh 1998; Hall et al. 2006). The $1.728\,\mathrm{d}^{-1}$ value used in our experiments is larger than the $0.5\,\mathrm{d}^{-1}$ value used in Hall et al. (2006) but similar to the $2\,\mathrm{d}^{-1}$ value Hall and Sardeshmukh (1998) argue is most consistent with observational estimates. The remaining terms represent sixth-order spatial diffusion. Although sixth-order diffusion as a function of the Courant number is implicit in the upwind-biased scheme used to evaluate the spatial derivatives (Wicker and Skamarock 2002), linearizing the equation set and setting $\bar{V}$ and $\bar{W}$ to zero eliminates this implicit diffusion in the meridional and vertical directions. Without diffusion, the meridional and vertical wavelengths of the disturbance collapse to the grid scale near the zero-wind line of the basic state flow, leading to unrealistically large shear, especially in the meridional direction. The additional diffusion in Eq. 18 crudely approximates the tendency of mixing by subgrid-scale turbulence to reduce this shear. Besides this effect, the overall structure and stability characteristics of the modal solutions of Exp. A are not overly sensitive to reasonable changes in the diffusion coefficients.

The desired normal-mode solutions to this system of linearized equations take the form

$$\psi'(\mathbf{r}, t) = \Re\{\hat{\psi}(y, z)e^{i(kx-\omega t)}\} = \Re\{\hat{\psi}(y, z)e^{ikx}e^{-i\omega t}\} \quad (19)$$

where ψ' represents a perturbation and all other variables have their standard meaning. To reach this solution, we initialize with random noise and integrate forward in time. During this integration, the zonal structure of ψ' is constrained to $\Re\{e^{ikx}\}$ using a discrete Fourier transform to isolate a single wavenumber of interest at every time step. With a sufficiently long integration time, the normal-mode structure $\Re\{\hat{\psi}(y, z)e^{-i\omega t}\}$ that maximizes the growth rate will eventually emerge. Because this modal structure grows exponentially, we periodically rescale it by a constant to maintain the perturbation fields within a physically realistic range.

In addition to obtaining the spatial structure of the normal modes, we also want to compare the growth rates for a wide range of normal modes with closely spaced wavelengths. The zonal wavelength as a function of wavenumber k is given by $L_x = N_x\frac{\Delta x}{k}$, where N_x is the number of grid points in the zonal direction and Δx the horizontal grid spacing. Since N_x and k can take on only integer values and Δx is held constant, calculating growth rates for a wide range of L_x values requires a large value of N_x and is thus computationally expensive. Therefore, instead of varying k to obtain the growth rates for different wavelengths, we hold k constant at wavenumber 2 and vary N_x. In other words, every simulated normal mode consists of exactly two full waves in the zonal direction and the length of the domain is increased or decreased to make the wavelength longer or shorter.

Although we will summarize the results of basic states from other longitudes, our primary focus will be at 87°E, which is located near the maximum track density of monsoon depressions (Fig. 2 in Hurley and Boos 2015). Figure 2 shows a latitude-height cross section of the basic state zonal winds and potential temperature (Fig. 2a) and the basic state absolute vorticity (Fig. 2b) at this longitude. The terrain is outlined in brown. The monsoon trough axis, as identified by the zero wind line between 20°N and 25°N, is associated with a maximum in absolute vorticity. As suggested by previous studies, the resulting vorticity gradient reversal could be barotropically unstable. Additionally, the transition from westerly monsoon flow at low levels to easterly flow aloft associated with the tropical easterly jet leads to strong vertical wind shear. As noted previously, its presence has led some to suggest that monsoon depressions may arise through baroclinic instability.

Several complications arise from using this basic state flow as given. One problem is the unphysical ERA-Interim data beneath the surface of the Himalayas, which can lead to growing normal

mode solutions not physically relevant to the atmosphere. To eliminate these spurious instabilities, we set $\bar{U}$ and $\bar{\theta}$ to latitude-independent values north of the dashed blue line in Fig. 2b. These constant values are a function of height only and are set equal to the values at the dashed blue line. An alternative would be to impose rigid-wall boundary conditions at the topography. However, in Exp. A we opt for the simpler treatment of boundary conditions that uses the approach just described. A second problem is that the most unstable normal mode for the range of basic states and wavelengths considered in this study is not always associated with the monsoon trough. At wavelengths longer than 3500 km, upper tropospheric waves dominate, and at wavelengths shorter than about 1000 km, waves grow near the surface along 10°N. Neither of these seems directly relevant to South Asian monsoon depressions, and the upper-tropospheric instabilities are shown in Section 4 to be an artifact of the zonally symmetric basic state. Thus, we exclude these wave modes by extending the model's upper and lateral boundaries in some of our calculations as far as needed to damp these instabilities, as shown by the dotted lines in Fig. 2b. Unfortunately, the upper-level damping comes uncomfortably close to the lower-tropospheric modes of interest to our study. For the part of our analysis where we show the structure of the wave modes, we present results for wavelengths short enough that upper-level damping is not required. For experiments that vary the wavelength and longitude, it is included.

3.2. *Results*

Results are shown in detail for the 87°E basic state for the normal mode of wavelength 3200 km, which is shorter than the most unstable mode but longer than that of typical monsoon depressions. Its horizontal structure in terms of pressure (p'), wind ($\mathbf{v}'$), and vertical velocity (w') is shown in Fig. 3. It consists of a series of cyclones and anticyclones that tilt against the basic state meridional shear, a configuration suggestive of barotropic instability. Their maximum amplitude lies near 25.7°N, which, given their westward phase velocity of $1.7\,\mathrm{m\,s^{-1}}$, is located near the critical layer of this basic state flow. Although this latitude is north of the observed maximum track density for monsoon depressions, which is located between 20°N and 23°N for 87°E (Fig. 1 in Hunt et al. (2016a)), significant amplitude does extend farther south. The pattern of ascent located west of the trough axis and descent to its east is broadly consistent with that of observed monsoon depressions.

The vertical structure of the disturbance is depicted in Fig. 4, which shows a longitude-height cross section of the meridional wind (v') and potential temperature (θ') at (a) 25.7°N, near the disturbance's maximum amplitude, and (b) 21.2°N, near where monsoon depressions more commonly track. Consistent with observed monsoon depressions, both cross sections have a warm over cold core with a low-level wind maximum. However, the 3.75 km altitude of the warm core at 25.7°N is much lower than the more typically observed value of 7-8 km (Fig. 13 in Hunt et al. (2016b)). The minimal to slightly downshear tilt with height indicates that these disturbances are not baroclinically unstable. In fact, most of their amplitude is confined to regions of weaker vertical shear.

Following the same procedure as above for different wavelengths using the 87°E basic state, we calculate the growth rate as a function of wavelength and use Eq. 16 to partition it into different physical processes (Fig. 5a). For a wide range of wavelengths, the meridional shear of the basic state zonal wind is barotropically unstable with the $u'v'\partial_y\bar{U}$ term contributing up to $0.62\,\mathrm{d^{-1}}$ to the growth rate (Fig. 5a). The net growth rate, however, is much lower with friction and diffusion consuming a large quantity of energy (Eq. 18). Diffusion, being scale selective, becomes an increasingly large energy sink at shorter wavelengths. As explicit diffusion is absent in the zonal direction, this trend reflects a shrinking meridional and vertical scale. Gradients in the zonal direction are, however, impacted by diffusion implicit in the upwind-biased numerical advection scheme. Being an unaccounted for energy sink, this process contributes to the residual becoming sharply negative at shorter wavelengths.

The pressure work term encompasses multiple physical processes whose combined impact on the total growth rate is negative for most wavelengths. The primary negative contribution comes from the energy needed to create the temperature perturbations associated with the circulation centers. As the wind perturbations grow by extracting energy from the basic state meridional shear, maintaining the resulting disturbance in approximate thermal wind balance requires that some of this kinetic energy be converted to potential energy through rising cool air and sinking warm air. There is some evidence that this process occurs in observed monsoon depressions: their center of circulation is often associated with sinking warm air (Warner 1984). In addition to consuming it, pressure work can generate kinetic energy through at least two distinct physical processes. One is the tendency for surface friction to angle the wind down the pressure gradient. A second is energy drawn from the basic state available potential energy, the energy source most commonly linked to baroclinic instability. However, given that the disturbance lacks an upshear tilt and that temperature and vertical velocity anomalies are in quadrature (Figs. 3 and 4), this process does not seem to be important. Interestingly, at shorter wavelengths, the pressure work becomes strongly positive. Given that the net pressure work is the sum of both positive and negative contributions, one possible explanation is that the substantially reduced barotropic conversion requires less kinetic energy to be converted to potential energy through pressure work. With this negative contributor reduced, the total becomes more positive. We also note that the smaller-scale disturbances become increasingly concentrated to the north, where the surface baroclinic zone is slightly stronger. In this region, it is possible that baroclinic conversion becomes a more important energy source.

Figure 5b shows the phase velocity and period as a function of wavelength. The phase speed is westward for all wavelengths and decreases in magnitude with increasing wavelength until around 4000 km. Afterwards it increases slightly before leveling off. Plots of the shorter wavelengths (not shown) reveal that they are increasingly embedded within the easterly flow to the north, a shift that would increase their westward phase speed. For wavelengths characteristic of monsoon depressions, the zonal phase velocity is between about -2.5 to -1.8 $\mathrm{m\,s^{-1}}$. By comparison, Boos et al. (2017) calculated a mean value of $-1.5\,\mathrm{m\,s^{-1}}$ and a mode value of $-3.4\,\mathrm{m\,s^{-1}}$ for observed monsoon depressions.

We repeat the procedure described in Sec. 3.1 to find normal mode solutions of 3200 km wavelength for a range of longitudes. To accomodate for the shifting latitude of the steepest topography and for the monsoon trough axis being located farther north as one moves westward, the model boundaries and damping regions (see Fig. 2) are shifted for each longitude following a similar logic as before. Figure 6 shows the growth rate as a function of longitude partitioned into different physical processes based on Eq. 16. This analysis reveals a wide range of longitudes that can support barotropic instability, with a sharp cutoff corresponding to the eastern and western edges of the monsoon trough (Fig. 1). As before, the net growth rate is small due to the effects of friction and diffusion. Although not shown, we note that normal modes obtained using basic states between 78°E and 92°E look very similar to those at 87°E that were discussed previously. However, west of this range, their structure changes. Between 74°E and 78°E, the wind anomalies of the modes become increasingly

elevated. This is reflected in the friction term becoming nearly zero and the pressure work term becoming strongly negative, a consequence of the loss of the positive source caused by low-level friction turning the wind down the pressure gradient. West of 74°E, the modes become increasingly baroclinic and surface intensified, exhibit an eastward phase velocity, and have little resemblance to those farther east. With this in mind, it is reasonable to conclude that the region that can support barotropic instability is approximately 20° (2200 km) long. The fact that this value is comparable to the wavelength of the most unstable normal modes (Fig. 5) motivates the next part of this study.

4. Zonally Varying Basic State (Exp. B)

As demonstrated in Exp. A, the longitudinal extent of the region that can support barotropic instability is of similar scale to or slightly shorter than the wavelengths at which normal modes grow fastest. With little separation between these two scales, it is questionable how relevant a zonally symmetric basic state is for disturbances that grow in the monsoon environment. In this experiment (Exp. B), we consider how zonal variations in the basic state impact the growth and structure of wave-like solutions to our linearized equation set.

4.1. *Experimental Design*

For perturbations linearized about a zonally-varying basic state, Eqs. 7a and 7b simplify to

$$\frac{\partial \mathbf{u}'}{\partial t} = -\bar{\mathbf{U}} \cdot \nabla \mathbf{u}' - \mathbf{u}' \cdot \nabla \bar{\mathbf{U}} - \nabla \phi' + g\frac{\theta'}{\theta_0}\hat{\mathbf{k}} - f\hat{\mathbf{k}} \times \mathbf{v}' + \mathbf{s}' \tag{20a}$$

$$\frac{\partial \theta'}{\partial t} = -\bar{\mathbf{U}} \cdot \nabla \theta' - \mathbf{u}' \cdot \nabla \bar{\theta} - w'\frac{d\theta_0}{dz} + s'_\theta \tag{20b}$$

Instead of the single-wavelength normal modes of Exp. A, solutions to these equations consist of cyclically repeating structures of the form

$$\psi'(\mathbf{r}, t) = e^{\sigma t}[A(\mathbf{r})sin(\omega t) + B(\mathbf{r})cos(\omega t)] \tag{21}$$

where σ is the growth rate and $A(\mathbf{r})$ and $B(\mathbf{r})$ represent two spatially orthogonal structures (Simmons et al. 1983; Hall and Sardeshmukh 1998). These solutions constitute the eigenmodes of this system of equations. Over the course of one wave period (ω^{-1}), they oscillate from A to $-B$ to $-A$ to B and then back again. As in Exp. A, over a sufficiently long integration time, the fields will converge to the fastest growing or slowest decaying eigenmode, depending on the sign of σ. Throughout the integration, we rescale the prognostic variables by a constant to keep them close to observed values. Specifically, all fields are renormalized every six hours such that the maximum pressure amplitude within the domain is set to 2 hPa. The terms $\mathbf{s}'$ and s'_θ are the same as in Exp. A except that an additional sixth-order diffusion term is added that acts in the zonal direction. Additional details of the model setup are listed in Tab. 1.

As in Exp. A, we have to account for the presence of topography and the artificial data beneath it. Since the technique used before does not extend well to zonal variations in topography, we take a different approach: the top faces of the control volumes lying just beneath the physical terrain are treated as the surface and the component of the fluxes in Eq. 10 orthogonal to the sides of the control volumes directly adjacent to the terrain are set to zero. This implementation leads to a stair-step like terrain. Although not optimal for simulating flow over complex topography, the fact that the effect of topography on the basic state is already included in the reanalysis mitigates some of the drawbacks of this approach.

A second problem we encountered was that small-scale spatial variability in the basic state leads to small-scale waves with higher growth rates than the ones in which we are interested. This problem is exacerbated by the presence of topography and the many regions of weak basic state flow. To damp these waves in favor of larger-scale ones, we increase the scale-selective sixth-order diffusion compared to the previous experiment (Tab. 1). Similar solutions can be reached with smaller amounts of diffusion, though they become increasingly contaminated with small-scale noise.

Finally, it is worth mentioning that, unlike in Exp. A, no upper-level wave modes appear in this experiment. As noted in Sec. 1, several studies found a most unstable mode in the upper-tropospheric flow (Shukla 1978; Goswami et al. 1980). This experiment suggests that they were artifacts of zonal symmetry.

4.2. *Results*

In contrast with Exp. A, the zonally varying basic state has no amplifying modal solutions. Hence, the structure that emerges after a sufficiently long integration is the slowest-decaying eigenmode. The time evolution of its pressure (p') and wind ($\mathbf{v}'$) over one wave period (12.7 days) overlaid with the basic state zonal wind ($\bar{U}$) is shown in Fig. 7. It forms a localized wave packet centered near the northernmost Bay of Bengal whose individual phases move northwestward along the monsoon trough axis. The individual circulation centers closely follow the path of observed monsoon depressions and, with their upshear tilt, bear some resemblance to the modal solutions in Exp. A. This similarity is especially apparent on days 0 and 6 when the maximum perturbation winds are centered within the region of maximum meridional shear. Significant wave amplitude also extends into regions east of 91°E. Considering the rapid dropoff in barotropic growth rates (Fig. 6) and their lack of upshear tilt, this extension is likely a dispersion phenomenon. With a poleward-directed absolute vorticity gradient (Fig. 2a) and westerly low-level flow (Fig. 1), the Rossby wave group velocity is eastward. This process would transport wave energy from the region of higher meridional shear in the west to regions of weaker shear in the east. Besides the monsoon depression-like wave modes, additional waves appear east of 100°E associated with a second region of enhanced meridional shear in the western Pacific (Fig. 1). These disturbances may correspond to easterly waves.

Figure 8 shows a cross section of the perturbation wind and potential temperature (θ') of the cyclonic phase of the wave at day 5. At this time, the disturbance is centered near 87°E, which is the longitude of focus in Exp. A. To account for its associated wind maxima being tilted with respect to lines of constant latitude, the fields are rotated 30° counterclockwise so that the cross section passes roughly through the middle of the cyclone along its direction of motion. This rotation allows for a better comparison with Exp. A. However, it should be noted that a degree of longitude in Fig. 8 corresponds to 0.87 of the unrotated value. To emphasize large scale features, the fields are averaged over three grid points (225 km) on either side of the cross section. The vertical structure of this disturbance is similar to that of both the most unstable normal mode in Exp. A and observed monsoon depressions; it has a warm-over-cold core structure with a wind maximum in the lower troposphere. However, the maximum amplitude of the warm core near 9 km is higher than that of the normal mode at 6.25 km (Fig. 4). For comparison, composites of monsoon depressions have a warm core maximum near 7.5 km (Fig. 13 in Hunt et al. 2016c), which lies midway between these two values.

Although our analysis focuses on their wind and temperature structure, perhaps one of the most notable features of monsoon

depressions is their ability to produce prodigious amounts of rain. As noted in Sec. 1, the condensational heating produced by this precipitation has long been established as an important energy source for their growth. Though we do not directly address how the depression-like wave modes isolated in our study interact with moist convection, we can use the distribution of vertical velocity to determine where precipitation would most likely occur. One benefit of such an analysis is that we can unambiguously diagnose the adiabatic contributions to vertical velocity absent the buoyant accelerations induced by condensational heating. Figure 9 shows the vertical velocity averaged from 1.0 to 5.0 km overlain with the winds ($\mathbf{v}'$) and pressure (p') at 3.25 km. It reveals a pattern of ascent to the west and descent to the east. Though the region of ascent is slightly farther north than typical, this pattern is broadly similar to that of observed monsoon depressions. This distribution of vertical velocity has generally been explained using quasi-geostrophic theory (e.g., Rao and Rajamani 1970; Rajamani and Rao 1981; Sanders 1984; Boos et al. 2015). Perhaps the easiest way to explain this pattern is that vorticity advection by a westward-directed thermal wind would lead to ascending motion downshear, or west, of the vortex. Idealized studies of vortices in background shear yield similar patterns of vertical velocity (Raymond 1992; Jones 2004), at least once the change in shear direction has been accounted for.

Besides providing a wind and temperature structure for the disturbance, the types of linear eigenmode analyses presented in this study are also useful for explaining its length scale. In a standard normal mode analysis (Eq. 19), solutions exist for a wide spectrum of wavenumbers, and it is generally assumed that the fastest growing normal mode dominates. By contrast, with a zonally varying basic state, solutions do not exist for arbitrary wavenumbers (Eq. 21). Instead, a preferred wavelength arises naturally. However, the wavelength and phase velocity fluctuate over the course of a wave period as the spatial structure oscillates between $A(\mathbf{r})$ and $B(\mathbf{r})$. Figure 10 shows this evolution as a function of time (Fig. 10b) along with the track of the cyclonic portion of the disturbance. Its path is labeled by day corresponding to Fig. 7 and shaded by the amplitude of its perturbation pressure. This amplitude being arbitrary, exact values are not given. The zonal wavelength is calculated by first smoothing the pressure field, finding the minimum and maximum pressure values of an adjacent trough and ridge, calculating the distance between them in the zonal direction, and then doubling this value to get a full wavelength. The gap in Fig. 10b coincides with the switch from using the ridge to the west of the cyclone to the one to the east.

Though somewhat north of average, the path of the cyclonic portion of the wave disturbance matches well with that of observed monsoon depressions, with its pressure anomaly reaching a maximum amplitude in the northern Bay of Bengal (Fig. 10a). The zonal wavelength varies from 1900 to 2600 km over the course of a full period, with an average value of 2100 km. This value compares well with the 2000-2500 km wavelength of observed monsoon depressions (Sikka (1977)) and is shorter than the most unstable mode isolated in Exp. A. We speculate that the length of the unstable region of the monsoon trough (∼2200 km in Exp. A) plays some role in setting this scale, though the close numerical similarity may be fortuitous. The zonal phase velocity also varies, with increases in magnitude roughly corresponding to decreases in wavelength. Its average over one period is $-2.0\,\mathrm{m\,s^{-1}}$, which lies between the mean ($-1.5\,\mathrm{m\,s^{-1}}$) and mode ($-3.4\,\mathrm{m\,s^{-1}}$) of observed monsoon depressions (Boos et al. (2017)). This velocity is somewhat slower than the $-3.1\,\mathrm{m\,s^{-1}}$ value of the normal mode corresponding to this wavelength. This discrepancy may result from the normal mode being more embedded within the easterly flow to the north. The average meridional velocity is $0.8\,\mathrm{m\,s^{-1}}$, which compares with a mean value of $1.0\,\mathrm{m\,s^{-1}}$ and a mode value of $1.7\,\mathrm{m\,s^{-1}}$ for observed monsoon depressions (Boos et al. (2017)). Thus, in general, the phase speed of this wave is on the slower end of observed values.

The growth rates for this disturbance over a full wave period are shown in Fig. 11. For clarity, the barotropic terms (Fig. 11a) are separated from the other terms (Fig. 11b). Consistent with Eq. 21, growth rates are oscillatory. They cycle twice per wave period because energy is a quadratic quantity. Similar to the normal mode solution, the $u'v'\partial_y\bar{U}$ term is the primary energy source. The two peaks in the growth rate correspond to the cyclone and anticyclone passing through the middle of the monsoon trough, a position that maximizes their interaction with the strongest meridional shear (Fig. 7). The only other positive contributor to K_p growth is from $u'u'\partial_x\bar{U}$, which results from the northwest-to-southeast tilt of the monsoon trough. This tilt leads to a zonal gradient of $\bar{U}$ that is acted upon by u'. All other terms in the K_p budget are small or negative. The largest energy sink comes from the artificial diffusion used to remove small-scale waves that would otherwise dominate the solution. Considering that this diffusion is likely overdone and contributes significantly to stabilizing this system, the total growth without this diffusion is also plotted in Fig. 11b. This can perhaps be regarded as an upper bound on the growth rate. Even with the effect of diffusion on the growth rate removed, the net growth rate over a full wave period is negative, though it does briefly become positive. To double check this interpretation, we ran an experiment with the explicit diffusion set to zero and confirmed that no growing waves emerge. Another term contributing to K_p loss is the residual, which, as previously discussed, results mostly from implicit diffusion. Altogether, factors leading to this wave decaying overwhelm those leading to its growth. Such a structure could not emerge spontaneously from small-amplitude perturbations as an instability would.

5. Non-Linear Initial Value Problem (Exp. C)

We now build upon the previous experiment by including the non-linear terms in our equation set. Since this basic state is stable to small perturbations and hence cannot support disturbances growing from small amplitude, we need an initial disturbance. Considering that the eastern Bay of Bengal is one of the most convectively active regions in the world during the summer monsoon, one possible source of an initial disturbance is a vortex created by condensational heating from convection. We envision such a transient heating event arising from the spontaneous aggregation of convection (e.g. Held et al. 1993; Wing et al. 2017), orographic lifting on the eastern edge of the Bay of Bengal (e.g. Xie et al. 2006; Grossman and Garcia 1990), or the formation of a squall line in the ambient shear. Zuidema (2003) documented a variety of organized convection over the Bay of Bengal, with the genesis of convection influenced by land-sea contrasts, the diurnal cycle, and the characteristic southward propagation of mesoscale disturbances within larger-scale synoptic systems. In this experiment (Exp. C), we investigate the response of our basic state to a heating impulse, remaining agnostic about its origin.

5.1. *Experimental Design*

This experiment uses the fully non-linear equation set with the zonally-varying basic state (Eq. 7). Details of the model setup are listed in Tab. 1. Since friction is a significant energy sink that substantially decreases growth rates in the linearized equations, it is useful to provide a more physically realistic calculation of its impact. No longer constrained by linearity, instead of the linear friction and artificial diffusion implemented in our previous experiments, we implement a simple first-order

turbulence closure with quadratic friction at the surface. To improve the representation of topography and energy dissipation within the boundary layer, we implement a stretched grid based on Anthes (1970). The vertical grid spacing varies from 50 m at the lowest level to 1000 m at the highest level. Repeating this experiment using linear friction as in Exp. A and Exp. B without grid stretching gives similar results, though the quadratic friction decreases growth rates slightly.

5.1.1. *Frictional Dissipation*

This experiment uses a simplified version of the Smagorinsky scheme based on the one implemented in the Weather Research and Forecasting Model (Skamarock et al. 2008). We set $\mathbf{s}'$ in Eq. 7a to

$$\mathbf{s}' = \frac{\partial \tau_u}{\partial z}\hat{\mathbf{i}} + \frac{\partial \tau_v}{\partial z}\hat{\mathbf{j}} \tag{22}$$

where τ_u and τ_v are the horizontal components of the stress vector induced by shear. They are defined as a time- and space-dependent mixing coefficient multiplied by the perturbation vertical shear,

$$\tau_u = K(\mathbf{r},t)\frac{\partial u'}{\partial z} \tag{23a}$$

$$\tau_v = K(\mathbf{r},t)\frac{\partial v'}{\partial z} \tag{23b}$$

The mixing coefficient K is a function of the vertical shear and static stability of the full velocity and temperature fields (i.e. basic state plus perturbation),

$$K = \left[l^2 C_s^2 \left(\frac{\partial u}{\partial z} + \frac{\partial v}{\partial z} \right)^2 - Pr^{-1}\frac{g}{\theta}\frac{\partial \theta}{\partial z} \right]^{\frac{1}{2}} \tag{24}$$

where l is equal to the vertical grid spacing, $C_s = 0.25$, and $Pr = 3$. The horizontal stress components at the surface are defined as

$$\tau_{u0} = C_D|\mathbf{v}|u \tag{25a}$$

$$\tau_{v0} = C_D|\mathbf{v}|v \tag{25b}$$

where C_D is the surface drag coefficient, which we set to 0.001 for water and 0.003 for land.

5.1.2. *Heating Impulse Structure*

We will represent the horizontal structure of the heating as a box oriented parallel to the monsoon trough as shown in Fig. 1. This particular shape was chosen based on our observation that convection over the Bay of Bengal often takes the form of lines oriented parallel to the shear. The vertical profile of this heating was obtained from Fig. 11 in Lin and Johnson (1996), which shows multiple heating profiles from observations of tropical oceanic convection, most of which have a maximum heating rate near 6 km. Specifically, we use the profile based on the results of Yanai et al. (1973). The magnitude of the heating is set to represent a rain rate of 6 $cm\ day^{-1}$ and is applied for 48 hours and then switched off. Applying it for a longer time period or for higher rain rates simply increases the magnitude of the resulting disturbance. The rate we have chosen produces disturbances with amplitudes comparable to those of observed monsoon depressions. Because the structure of the resulting disturbance can partially be attributed to the heating, independent of the basic state, we will also show results for the heating applied to a resting basic state.

5.2. *Results*

The time evolution of the resulting disturbance is depicted in Fig. 12, which shows the pressure (p'), wind ($\mathbf{v}'$), and basic state zonal wind ($\bar{U}$) at 2, 3, and 4 days into the simulation at 3.1 km above sea level. The heating impulse generates a vortex that disperses into a wave and weakens with time as it moves westward. Its average motion over this time period is northwestward (300°) at $2.8\,\mathrm{m\,s^{-1}}$. As in Exp. B, the wavelength varies with time and longitude. For a lower bound, taking the distance on day 3 between the center of the westernmost anticyclone and cyclone as a half wavelength yields a full wavelength of 1600 km, and taking the distance between the two anticyclones yields a wavelength of 2000 km. As an upper bound, taking the distance between the cyclone and easternmost anticyclone at day 4 as a half wavelength yields a full wavelength of approximately 2500 km. These values are within the range of Exp. B (Fig. 10b) and are shorter than the most unstable normal mode (Fig. 5). The same fields for the disturbance in the resting basic state are plotted in Fig. 13. By comparison, it is smaller, weaker, and does not evolve into a wave. The diameter of maximum wind is about 225 km at day 3, a size typical of a mesoscale convective vortex but much smaller than the disturbance in the monsoon basic state. Its velocity is north-northwestward at $1.4\,\mathrm{m\,s^{-1}}$, which is slower than in the monsoon basic state. With no background flow to advect it, this motion is best explained by the so-called "beta effect", which relies on the planetary vorticity gradient.

We now examine the vertical structure of the two disturbances in terms of wind and potential temperature (θ') using longitude-height cross sections (Fig. 14). As in Exp. B, the fields for the disturbance in the monsoon basic state are rotated 30° counterclockwise so that the cross section passes roughly through the middle of the cyclone and westernmost anticyclone. The cross section for the resting basic state also passes through the cyclone center but is not rotated. To emphasize the broader scale circulation features, the fields are averaged over 150 km on either side of the cross section. Results for the monsoon basic state are shown in Fig. 14a and for the resting basic state in Fig. 14b. Because the disturbance in the resting state has greater amplitude in the upper troposphere, the vertical scale of Fig. 14b is expanded relative to that of Fig. 14a.

The disturbance in the monsoon basic state has a warm-over-cold core vertical structure with a wind maximum near 3 km. This pattern is broadly similar to that of the previous experiments (Fig. 4b and Fig. 8), though the warm core is centered about 3 km lower compared to the disturbance in the linearized zonally varying basic state. The disturbance in the resting basic state is notably different. In contrast with the disturbance in the monsoon basic state, it has a wind maximum in the upper troposphere associated with anticyclonic flow induced by the negative vertical gradient of heating aloft. The strong easterly shear associated with the tropical easterly jet might prevent disturbances from extending above the mid-troposphere; the near-zero absolute vorticity in the upper-tropospheric Asian monsoon anticyclone would also prevent divergence from generating anticyclonic anomalies at those levels. In any case, the disturbance that forms in the resting basic state also exhibits a warm-over-cold core structure in the lower and middle troposphere, though the temperature anomalies are much weaker. The fact that the disturbance in the monsoon basic state (Fig. 14a) and the one in the resting basic state (Fig. 14b) both have a warm-over-cold core structure suggests that the heating profile excites and constructively interferes with the least stable wave modes of the monsoon basic state isolated in Exp. B. The fact that the imposed heating profile has no cooling at low levels suggests that the cold core can be at least partially

attributed to cooling by ascent forced by frictional convergence near the vortex center.

Once again, we examine vertical velocity to diagnose where precipitation would most likely be concentrated by the dry dynamics. Figure 15 shows the vertical velocity averaged from 1.0 to 5.0 km overlain with the winds ($\mathbf{v}'$) and pressure (p') at 3.1 km. Similar to Exp. B, ascent occurs to the west and descent to the east. However, the ascent is now concentrated more toward the southwest, in better agreement with observations. These results are consistent with the rainfall in monsoon depressions being biased toward the southwest corner of their circulation.

Figure 16 shows the energy budget for this experiment based on Eq. 16. We include time series of both the mass-weighted average of various terms (Fig. 16a) and the growth rates (Fig. 16b). To simplify the analysis, we note that some of the barotropic terms represent essentially the same process rotated 90° and can be grouped together. We will call these new combined terms the horizontal shear term ($u'v'\partial_y\bar{U} + u'v'\partial_x\bar{V}$), the horizontal convergence term ($u'^2\partial_x\bar{U} + v'^2\partial_y\bar{V}$), and the vertical shear term ($u'w'\partial_z\bar{U} + v'w'\partial_z\bar{V}$).

Because the heating source is switched off after 48 hours, it is best to consider the periods before and after this time separately. During the first 48 hours, while the heating is being applied, the largest term is pressure work. This is a reflection of the drop in hydrostatic pressure caused by the heating, which in turn accelerates the perturbation wind. The second largest source of K_p is associated with the vertical shear. This energy comes primarily from the vertical velocity induced by the heating transporting eastward momentum upward. Recall that neither of these two terms were significant sources of K_p in the normal mode (Fig. 5); both result from the interaction of the imposed heating with the basic state. While the heating is being applied, K_p generation from horizontal shear and horizontal convergence also increase. In addition to these K_p sources, friction, advection, and the residual serve as energy sinks. As noted previously, the residual most likely results from numerical diffusion implicit in the fifth-order advection scheme.

After the heating is switched off, the energetics more closely resemble that of Exps. A and B. Without the vertical velocity and hydrostatic pressure falls forced by the heating, the vertical shear and pressure work terms become negative. By contrast, the horizontal shear term emerges as the largest source of K_p with only minor contributions from horizontal convergence. However, similar to Exp. B, it is not undergoing unstable growth. Although its growth rate from horizontal shear is similar to that of the most unstable normal mode at $0.5\,\mathrm{d}^{-1}$, the energy sources approximately balance the energy sinks. This balance leads to several days of near steady K_p with a slow decline afterward. Nevertheless, even if stable, this disturbance still draws substantial amounts of energy from the basic state shear.

5.3. *Sensitivity to Heating Location*

Although reasonable increases in the size and amplitude of the heating impulse simply result in a larger amplitude disturbance, the sensitivity of the response to heating location is much more interesting. To explore this, Exp. C is repeated in a series of integrations where the heating region is centered at every point on a 200 km by 200 km grid within a rectangle bounded to the south and north by latitudes 11.3°N and 27.5°N and to the west and east by 70.7°E and 105.7°E. This layout results in 200 different experiments. To summarize these experiments, we calculate the total amount of K_p produced by various physical processes by integrating the rate of K_p generation for selected terms in Eq. 16. These values are then plotted on a map at the center of each heating parallelogram. The resulting map shows the domain-integrated perturbation kinetic energy generated as a response to the heating applied at each location. We will split our analysis into two time periods: one limited to the first 48 hours of the simulation, during which the heating is being applied (contours in Fig. 17), and one from 51 to 144 hours, during which the heating has been switched off (shading in Fig. 17).

During the first 48 hours of simulation, K_p production is dominated by the pressure work and vertical shear terms throughout many of the experiments (Fig. 17). As the vertical shear term reflects upward momentum transport by the vertical velocity induced by the heating, it is highest in the southwest part of the domain where the basic state vertical shear is largest. However, on closer inspection, this extra K_p does not ultimately lead to stronger vortices; it is more indicative of the disturbance being sheared apart and hence is probably not an important energy source for monsoon depressions. What does appear important, however, is the pressure work term, which is maximized when heating is applied within the monsoon trough. This pattern can perhaps best be explained by understanding how the basic state affects the Rossby radius of deformation, which can be defined as

$$L_R = \frac{NH}{\bar{\zeta} + \zeta' + f} \tag{26}$$

where N is the Brunt-Vaisala frequency, H is the depth scale, $\bar{\zeta}$ and ζ' are the basic state and perturbation relative vorticity, and f is the planetary vorticity. Where the deformation radius is small, temperature perturbations generated by heating are more efficiently converted to perturbation kinetic energy associated with balanced flow.

Within the monsoon trough, L_R is smallest due to the combined effects of $\bar{\zeta}$ being larger from the enhanced meridional shear and f being larger due to the monsoon trough's more northerly location within the domain. Additionally, because a vortex forming within the weaker vertical shear of the monsoon trough will not be sheared apart as quickly, the increasing perturbation vorticity (ζ') will further decrease L_R. An equivalent explanation is that the rate of vorticity production by vertical stretching will be highest where the absolute vorticity (i.e. $\bar{\zeta} + \zeta' + f$) is largest. Taken alone, this analysis may appear to suggest that vortex formation frequency—and by extension, monsoon depression frequency—from convective heating is nearly uniform along the monsoon trough axis with a maximum in the northwest. However, it should be noted that, although the heating rates in our experiments are held constant, precipitation is climatologically much higher toward the southeastern end of the monsoon trough. Including this factor would presumably shift the maximum more toward the Bay of Bengal, where observed monsoon depression frequency is highest.

After 48 hours, the heating is switched off and the disturbance freely evolves within the basic state flow, with various processes contributing to K_p production (Fig. 17). In contrast with the previous 48 hours, K_p growth from horizontal shear is by far the dominant term. This growth is concentrated in two regions: one in the northernmost Bay of Bengal and adjacent land areas and one in the northwestern monsoon trough. The former coincides closely with the observed maximum track density of monsoon depressions (Fig. 6a in Hurley and Boos 2015) and suggests that convection in the northernmost Bay of Bengal is especially favorable for monsoon depression growth. The region in which a heating impulse leads to strong growth through horizontal shear is localized because the basic state shear becomes more barotropically stable to the east (Fig. 6), and because disturbances forming to the northwest are quickly advected out of the region of highest meridional shear. The second maximum in energy conversion lies in a relatively dry region over northwestern India that has a much lower track

density for monsoon depressions but a higher track density for shallow, non-precipitating vortices trapped in the lower troposphere (Hurley and Boos 2015; Ditchek et al. 2016). As it is colocated with a region of increased pressure work (Fig. 17d), disturbances in this region may grow from both baroclinic and barotropic processes. This is consistent with Fig. 6 from Exp. A.

6. Discussion and Conclusions

Though far from complete, this set of idealized experiments provides a starting point for understanding the basic dynamics of monsoon depressions. To the extent that the dynamics of these storms can be explained by linear instability theory, our results suggest that barotropic instability is most relevant. In the simplest case of a zonally symmetric basic state, it yields a most unstable normal mode that reproduces many of the observed features of monsoon depressions, including their warm-over-cold core structure, low-level wind maximum, and slow, westward propagation. However, given that these modes are similar in length to the part of the monsoon trough that can support barotropic instability, a zonally varying basic state seems more relevant. In this case, a linear instability analysis reveals wave modes whose structure and energetics closely resemble those of the normal mode solutions, but which decay with time as barotropic energy conversion is unable to overcome energy lost through dissipative processes. The approximately 2100 km wavelength of this least stable mode is shorter than that of the most unstable normal mode and in close agreement with observed monsoon depressions. Although such a decaying mode would not develop spontaneously, it can be forced by applying a localized heating impulse within the monsoon trough with a vertical profile representative of oceanic moist convection. The amount of energy extracted through barotropic conversion is maximized when this heating is placed in the northernmost Bay and Bengal and adjacent landmass to the west. Additionally, consistent with recent work (Cohen and Boos 2016), we find no baroclinic instability. In fact, in most of our simulations, the opposite occurs: perturbation kinetic energy is transformed into potential energy associated with temperature perturbations through the pressure work term. Of course, our experiments alone cannot dismiss the possibility of moist baroclinic instability as they did not include the effects of condensational heating from precipitation.

As discussed in the introduction, support for barotropic instability in past literature is mixed. Some studies find significant disagreement between the structure of barotropic instabilities and observed monsoon depressions while others find barotropic energy conversion to be insignificant in their energetics. Here we address some of these issues. The main studies that successfully isolated barotropically unstable modes in the mid-tropospheric flow find disturbances whose phase velocity is in the wrong direction (Nitta and Masuda 1981; Subrahmanyam et al. 1981). This discrepancy could result from the use of two-dimensional models in those studies, which neglect the large vertical variations in the basic state flow. Even though barotropic instability is at its simplest a two-dimensional phenomenon, these variations may be important for the phase velocity. On the other hand, previous studies finding unstable normal modes in the upper troposphere (Shukla 1978; Goswami et al. 1980) are partially consistent with our results; in order to isolate lower-tropospheric modes with wavelengths longer than about 3500 km, we had to damp the faster growing upper-tropospheric modes. Our results suggest that these upper-tropospheric waves are artifacts of a zonally symmetric basic state, since they do not appear in the zonally varying basic state. Of course, some of the discrepancies may stem from the particular choice of basic state. This possibility is somewhat more difficult to assess, but our choice of basic state is arguably more realistic than the idealized profiles used in many prior studies (e.g. Lindzen et al. 1983; Nitta and Masuda 1981); in a brief sensitivity analysis (described in the Methods section), we furthermore found that an alternate basic state obtained from an EOF analysis did not yield growing disturbances for any of our experiments.

A seemingly more significant problem is that our results appear to run contrary to a number of observational studies that come to the opposite conclusion: energy is transferred from the perturbation flow associated with monsoon depressions to the larger-scale monsoon trough (Rajamani 1985; Rajamani and Sikdar 1989; Krishnamurti et al. 2013). However, this disagreement probably results from the different methods used to assess this transfer. Whereas we calculate transfer between a perturbation and a time-independent basic state, previous studies have used a zonal-mean eddy decomposition (Lorenz 1967). There are a number of problems with this latter approach. First, although it is valid only for a global domain, prior studies of monsoon depressions apply it over a domain limited to the monsoon region. Therefore, any conclusions from such an analysis should be approached with caution. Second, since the monsoon trough itself exhibits large deviations from the zonal mean, its energetics would contribute significantly to the eddy flow. Consequently, such a decomposition would not properly separate monsoon depressions from the monsoon trough. In fact, with its northwest-to-southeast orientation, the monsoon trough tilts downshear relative to the zonal mean flow, a configuration that would contribute negatively to the barotropic energy conversion term and potentially overwhelm any positive contribution from an upshear-tilted monsoon depression. Finally, the zonal-mean or time-mean eddy decomposition traditionally used in observational studies would yield slightly different results compared with idealized modeling studies that use a time-independent basic state. For barotropic instability, this averaging would reduce the meridional shear since it would include the tendency of the growing disturbance to stabilize the flow.

Though not the main focus of this study, our experiments can contribute some value to the discussion of why monsoon depressions move northwestward, a topic that has received considerable attention over the years due to the apparent propagation of these storms against the westerly monsoon flow. A key result is that all of the wave modes we have isolated have a westward or northwestward phase velocity. To the extent that they can describe monsoon depressions, it supports the hypothesis that the direction of propagation can be explained by adiabatic dynamics alone (Boos et al. 2015). As such, our results are inconsistent with the argument that vortex stretching by convection is necessary for their westward propagation (Daggupaty and Sikka 1977; Chen et al. 2005; Adames and Ming 2018b). Nevertheless, in the real atmosphere, a variety of mechanisms likely contributes to their overall motion, including the impact of moist convection, interaction with the Himalayas (Hunt and Parker 2016), or non-linear advection (Boos et al. 2015). Indeed, as the phase velocities in our experiments are somewhat slower than typically observed, it is possible that one or more of these processes could make up for the difference.

Regardless of how closely the resulting wave modes may resemble monsoon depressions, several deficiencies make the mechanisms presented in this study an incomplete explanation of the origin and amplification of these storms. First, since net growth rates are negative for the zonally varying basic states, such structures could not emerge spontaneously from small, random perturbations as in traditional instability theories. We can provide some speculation on ways to resolve this issue. One possibility is that the monsoon trough briefly reaches a state of barotropic instability before being stabilized by the growing disturbance. Although our technique to construct a representative basic state

aimed to retain the strong meridional shear, perhaps an even shorter averaging period would lead to a barotropically unstable basic state. On the other hand, if instability is rare, an initial disturbance of sufficient amplitude is needed. It has been argued that monsoon depressions often have upstream predecessors, such as easterly waves or typhoons from the western Pacific (Chen and Weng 1999). The increased shear in the monsoon trough could allow these disturbances to reamplify. Nevertheless, they are often observed to develop *in situ*, with no apparent precursor. The results from Exp. C suggest that, even for a stable basic state, convection concentrated in the Bay of Bengal can generate a vortex that projects onto the linear wave mode isolated in Exp. B. Although its net growth rate is near zero, it still extracts energy from the background meridional shear, preventing its decay as it propagates across India for several days. Though we offer no verification that such a process occurs in nature, considering that the eastern Bay of Bengal is one of the most convectively active regions in the world during summer, it seems at least plausible. This argument is similar to some hypotheses for the origin of African easterly waves (Hall et al. 2006; Thorncroft et al. 2008). The monsoon trough may be particularly favorable because of its high inertial stability, which leads to efficient conversion of diabatic heating to kinetic energy.

A separate but related problem is that, even if one of the mechanisms listed above can initiate a disturbance, how does it continue to grow? This is where we speculate that condensational heating from precipitation is important. The structures generated in our experiments have a relatively deep, concentrated region of ascent to the west or southwest of the cyclonic vortex. Because this ascent exists independent of buoyant accelerations caused by moist convection, it can organize precipitation, and the associated condensational heating can generate kinetic energy. This heating will lead to growth of the initial disturbance if it is positively correlated with the perturbation temperature. This scenario would provide a role for the vertical shear: a vortex drawing energy from horizontal shear and interacting with vertical shear produces strong vertical velocity that can organize precipitation. In summary, most other studies of monsoon depression energetics have established diabatic heating by cumulus convection as the primary energy source. We argue that the wave modes isolated in our experiments provide the organizing structure needed for monsoon depression amplification, even if condensational heating is a larger source of energy. After all, cumulus convection may be ubiquitous, but monsoon depressions are not: even in South Asia, they undergo genesis and growth in a very confined geographic region.

Acknowledgement

This work was supported by National Science Foundation award AGS-1746160, Office of Naval Research award N00014-15-1-2531, and the U.S. Department of Energy, Office of Science, Biological and Environmental Research under Award Number DE-SC0019367. Model integrations used the Savio computational cluster provided by Berkeley Research Computing at the University of California, Berkeley.

References

Adames, Á. F. and Ming, Y. (2018a) Interactions between water vapor and potential vorticity in synoptic-scale monsoonal disturbances: Moisture vortex instability. *Journal of the Atmospheric Sciences*, **75**, 2083–2105.

— (2018b) Moisture and moist static energy budgets of South Asian monsoon low pressure systems in GFDL AM4.0. *Journal of the Atmospheric Sciences*, **75**, 2107–2123.

Anthes, R. A. (1970) Numerical experiments with a two-dimensional horizontal variable grid. *Monthly Weather Review*, **98**, 810–822.

Arakawa, A. and Lamb, V. R. (1977) Computational design of the basic dynamical processes of the UCLA general circulation model. *Methods in Computational Physics*, **17**, 173–265.

Arndt, D. S., Basara, J. B., McPherson, R. A., Illston, B. G., McManus, G. D. and Demko, D. B. (2009) Observations of the overland reintensification of tropical storm Erin (2007). *Bulletin of the American Meteorological Society*, **90**, 1079–1093.

Bannon, P. R. (1995) Potential vorticity conservation, hydrostatic adjustment, and the anelastic approximation. *Journal of the Atmospheric Sciences*, **52**, 2302–2312.

Boos, W., Hurley, J. and Murthy, V. (2015) Adiabatic westward drift of Indian monsoon depressions. *Quarterly Journal of the Royal Meteorological Society*, **141**, 1035–1048.

Boos, W. R., Mapes, B. E. and Murthy, V. S. (2017) Potential vorticity structure and propagation mechanism of Indian monsoon depressions. In *The Global Monsoon System: Research and Forecast*, 187–199. World Scientific.

Chen, T.-C. and Weng, S.-P. (1999) Interannual and intraseasonal variations in monsoon depressions and their westward-propagating predecessors. *Monthly Weather Review*, **127**, 1005–1020.

Chen, T.-C., Yoon, J.-H. and Wang, S.-Y. (2005) Westward propagation of the Indian monsoon depression. *Tellus A*, **57**, 758–769.

Chorin, A. J. (1968) Numerical solution of the Navier-Stokes equations. *Mathematics of computation*, **22**, 745–762.

Cohen, N. Y. and Boos, W. R. (2016) Perspectives on moist baroclinic instability: implications for the growth of monsoon depressions. *Journal of the Atmospheric Sciences*, **73**, 1767–1788.

Daggupaty, S. M. and Sikka, D. R. (1977) On the vorticity budget and vertical velocity distribution associated with the life cycle of a monsoon depression. *Journal of the Atmospheric Sciences*, **34**, 773–792.

Dee, D. P., Uppala, S., Simmons, A., Berrisford, P., Poli, P., Kobayashi, S., Andrae, U., Balmaseda, M., Balsamo, G., Bauer, P. et al. (2011) The ERA-interim reanalysis: Configuration and performance of the data assimilation system. *Quarterly Journal of the Royal Meteorological Society*, **137**, 553–597.

Ditchek, S. D., Boos, W. R., Camargo, S. J. and Tippett, M. K. (2016) A genesis index for monsoon disturbances. *Journal of Climate*, **29**, 5189–5203.

Goswami, B., Keshavamurty, R. and Satyan, V. (1980) Role of barotropic, baroclinic and combined barotropic-baroclinic instability for the growth of monsoon depressions and mid-tropospheric cyclones. *Proceedings of the Indian Academy of Sciences-Earth and Planetary Sciences*, **89**, 79–97.

Grossman, R. L. and Garcia, O. (1990) The distribution of deep convection over ocean and land during the asian summer monsoon. *Journal of climate*, **3**, 1032–1044.

Hall, N. M., Kiladis, G. N. and Thorncroft, C. D. (2006) Three-dimensional structure and dynamics of african easterly waves. Part II: Dynamical modes. *Journal of the Atmospheric Sciences*, **63**, 2231–2245.

Hall, N. M. and Sardeshmukh, P. D. (1998) Is the time-mean Northern Hemisphere flow baroclinically unstable? *Journal of the Atmospheric Sciences*, **55**, 41–56.

Held, I. M., Hemler, R. S. and Ramaswamy, V. (1993) Radiative-convective equilibrium with explicit two-dimensional moist convection. *Journal of the atmospheric sciences*, **50**, 3909–3927.

Hunt, K. M. and Parker, D. J. (2016) The movement of Indian monsoon depressions by interaction with image vortices near the Himalayan wall. *Quarterly Journal of the Royal Meteorological Society*, **142**, 2224–2229.

Hunt, K. M., Turner, A. G., Inness, P. M., Parker, D. E. and Levine, R. C. (2016a) On the structure and dynamics of Indian monsoon depressions. *Monthly Weather Review*, **144**, 3391–3416.

Hunt, K. M., Turner, A. G. and Parker, D. E. (2016b) The spatiotemporal structure of precipitation in Indian monsoon depressions. *Quarterly Journal of the Royal Meteorological Society*, **142**, 3195–3210.

— (2016c) The spatiotemporal structure of precipitation in Indian monsoon depressions. *Quarterly Journal of the Royal Meteorological Society*, **142**, 3195–3210.

Hurley, J. V. and Boos, W. R. (2015) A global climatology of monsoon low-pressure systems. *Quarterly Journal of the Royal Meteorological Society*, **141**, 1049–1064.

Jones, S. C. (2004) On the ability of dry tropical-cyclone-like vortices to withstand vertical shear. *Journal of the Atmospheric Sciences*, **61**, 114–119.

Kasture, S., Keshavamurty, R. and Satyan, V. (1993) A model study of the growth of summer monsoon disturbances. *Current Science*, 673–679.

Keshavamurty, R. (1972) On the vertical tilt of monsoon disturbances. *Journal of the Atmospheric Sciences*, **29**, 993–995.

Krishnakumar, V., Keshavamurty, R. and Kasture, S. (1992) Moist baroclinic instability and the growth of monsoon depressionslinear and nonlinear

studies. *Proceedings of the Indian Academy of Sciences-Earth and Planetary Sciences*, **101**, 123–152.

Krishnamurti, T., Kanamitsu, M., Godbole, R., Chang, C.-B., Carr, F. and Chow, J. H. (1976) Study of a monsoon depression (ii), dynamical structure. *Journal of the Meteorological Society of Japan. Ser. II*, **54**, 208–225.

Krishnamurti, T., Martin, A., Krishnamurti, R., Simon, A., Thomas, A. and Kumar, V. (2013) Impacts of enhanced CCN on the organization of convection and recent reduced counts of monsoon depressions. *Climate Dynamics*, **41**, 117–134.

Krishnamurti, T., Molinari, J., Pan, H.-l. and Wong, V. (1977) Downstream amplification and formation of monsoon disturbances. *Monthly Weather Review*, **105**, 1281–1297.

Lin, X. and Johnson, R. H. (1996) Heating, moistening, and rainfall over the western pacific warm pool during TOGA COARE. *Journal of the Atmospheric Sciences*, **53**, 3367–3383.

Lindzen, R., Farrell, B. and Rosenthal, A. (1983) Absolute barotropic instability and monsoon depressions. *Journal of the Atmospheric Sciences*, **40**, 1178–1184.

Lorenz, E. (1967) *The nature and theory of the general circulation of the atmosphere*, vol. 218. World Meteorological Organization Geneva.

Mishra, S. (2018) On the evolution of planetary-scale fields and genesis of monsoon depressions over the Indian region. *Quarterly Journal of the Royal Meteorological Society*, **144**, 129–141.

Mishra, S. and Salvekar, P. (1980) Role of baroclinic instability in the development of monsoon disturbances. *Journal of the Atmospheric Sciences*, **37**, 383–394.

Montgomery, M. T. and Smith, R. K. (2014) Paradigms for tropical cyclone intensification. *Australian Meteorological and Oceanographic Journal*, **64**, 37–66.

Moorthi, S. and Arakawa, A. (1985) Baroclinic instability with cumulus heating. *J. Atmos. Sci.*, **42**, 2007–2031.

Nagar, S., Bawiskar, S., Chinthalu, G. and Kulkarni, J. (2009) Study of dynamical structure of an unusual monsoon depression formed over the Bay of Bengal during August 2006. *Pure and Applied Geophysics*, **166**, 485–507.

Nitta, T. and Masuda, K. (1981) Observational study of a monsoon depression developed over the Bay of Bengal during summer MONEX. *Journal of the Meteorological Society of Japan. Ser. II*, **59**, 672–682.

Orlanski, I. and Chang, E. K. (1993) Ageostrophic geopotential fluxes in downstream and upstream development of baroclinic waves. *Journal of the Atmospheric Sciences*, **50**, 212–225.

Rajamani, S. (1985) Energetics of the monsoon circulation over south Asia. ii. energy terms and energy transformation terms. *Mausam*, **36**, 405–412.

Rajamani, S. and Rao, K. (1981) On the occurrence of rainfall over southwest sector of monsoon depression. *Mausam*, **32**, 215–220.

Rajamani, S. and Sikdar, D. (1989) Some dynamical characteristics and thermal structure of monsoon depressions over the Bay of Bengal. *Tellus A: Dynamic Meteorology and Oceanography*, **41**, 255–269.

Rao, K. and Rajamani, S. (1970) Diagnostic study of a monsoon depression by geostrophic baroclinic model. *Indian Journal of Meteorology and Geophysics*, **21**, 187–194.

Rao, V. B. (1971) Dynamic instability of the zonal current during a break monsoon. *Tellus*, **23**, 111–112.

Raymond, D. (1992) Nonlinear balance and potential-vorticity thinking at large Rossby number. *Quarterly Journal of the Royal Meteorological Society*, **118**, 987–1015.

Saha, K. and Chang, C. (1983) The baroclinic processes of monsoon depressions. *Monthly Weather Review*, **111**, 1506–1514.

Saha, K., Sanders, F. and Shukla, J. (1981) Westward propagating predecessors of monsoon depressions. *Monthly Weather Review*, **109**, 330–343.

Salvekar, P., George, L. and Mishra, S. (1986) Low level wind shear and baroclinic growth of monsoon depression scale waves. *Meteorology and Atmospheric Physics*, **35**, 10–18.

Salvekar, P. and Mishra, S. (1985) Baroclinic energetics and zonal plane distribution of monsoon disturbances. *Pure and Applied Geophysics*, **123**, 448–462.

Sanders, F. (1984) Quasi-geostrophic diagnosis of the monsoon depression of 5–8 July 1979. *Journal of the Atmospheric Sciences*, **41**, 538–552.

Shukla, J. (1977) Barotropic-baroclinic instability of mean zonal wind during summer monsoon. *Pure and Applied Geophysics*, **115**, 1449–1461.

— (1978) CISK-barotropic-baroclinic instability and the growth of monsoon depressions. *Journal of the Atmospheric Sciences*, **35**, 495–508.

Sikka, D. (1977) Some aspects of the life history, structure and movement of monsoon depressions. *Pure and Applied Geophysics*, **115**, 1501–1529.

Simmons, A., Wallace, J. and Branstator, G. (1983) Barotropic wave propagation and instability, and atmospheric teleconnection patterns. *Journal of the Atmospheric Sciences*, **40**, 1363–1392.

Skamarock, W. C., Klemp, J. B., Dudhia, J., Gill, D. O., Barker, D. M., Wang, W. and Powers, J. G. (2008) A description of the advanced research WRF version 3. NCAR technical note -475+STR.

Subrahmanyam, D., Tandon, M., George, L. and Mishra, S. (1981) Role of barotropic mechanism in the development of a monsoon depression: A MONEX study. *Pure and Applied Geophysics*, **119**, 901–912.

Thorncroft, C. D., Hall, N. M. and Kiladis, G. N. (2008) Three-dimensional structure and dynamics of African easterly waves. Part III: Genesis. *Journal of the Atmospheric Sciences*, **65**, 3596–3607.

Warner, C. (1984) Core structure of a Bay of Bengal monsoon depression. *Monthly Weather Review*, **112**, 137–152.

Wicker, L. J. and Skamarock, W. C. (2002) Time-splitting methods for elastic models using forward time schemes. *Monthly Weather Review*, **130**, 2088–2097.

Wing, A. A., Emanuel, K., Holloway, C. E. and Muller, C. (2017) Convective self-aggregation in numerical simulations: a review. *Surv. Geophys.*, 1–25.

Xie, S. P., Xu, H., Saji, N. H., Wang, Y. and Liu, W. T. (2006) Role of narrow mountains in large-scale organization of Asian Monsoon convection. *J. Clim.*, **19**, 3420–3429.

Yanai, M., Esbensen, S. and Chu, J.-H. (1973) Determination of bulk properties of tropical cloud clusters from large-scale heat and moisture budgets. *Journal of the Atmospheric Sciences*, **30**, 611–627.

Zuidema, P. (2003) Convective clouds over the bay of bengal. *Monthly Weather Review*, **131**, 780–798.

Table 1. Model Parameters

	Experiment A	Experiment B	Experiment C
Equation Set	Linear	Linear	Non-Linear
Horizontal Spacing ($\Delta x = \Delta y$)	100 km	75 km	50 km
Vertical Spacing (Δz)	500 m	500 m	Stretched
Time Step (Δt)	600 s	450 s	300 s
Grid Points (N_x, N_y, N_z)	variable, 40, 40	95, 46, 42	140, 65, 40
Latitude Range	1° - 36°N	3° - 32°N	6° - 35°N
Longitude Range	Fixed Value	55° - 120°E	50° - 115°E
Horizontal Diffusion (α_x,α_y)	0, 1.2×10^{-3}	1.2×10^{-2}, 1.2×10^{-2}	No explicit
Vertical Diffusion (α_z)	1.2×10^{-4}	1.2×10^{-3}	Flow based 2nd Order
Surface Friction (s_0, s^{-1})	2×10^{-5}	2×10^{-5}	Quadratic Drag
Boundary Width (B) (north, south, east, west)	10, 6, periodic	5, 5, 5, 5	5, 5, 5, 5

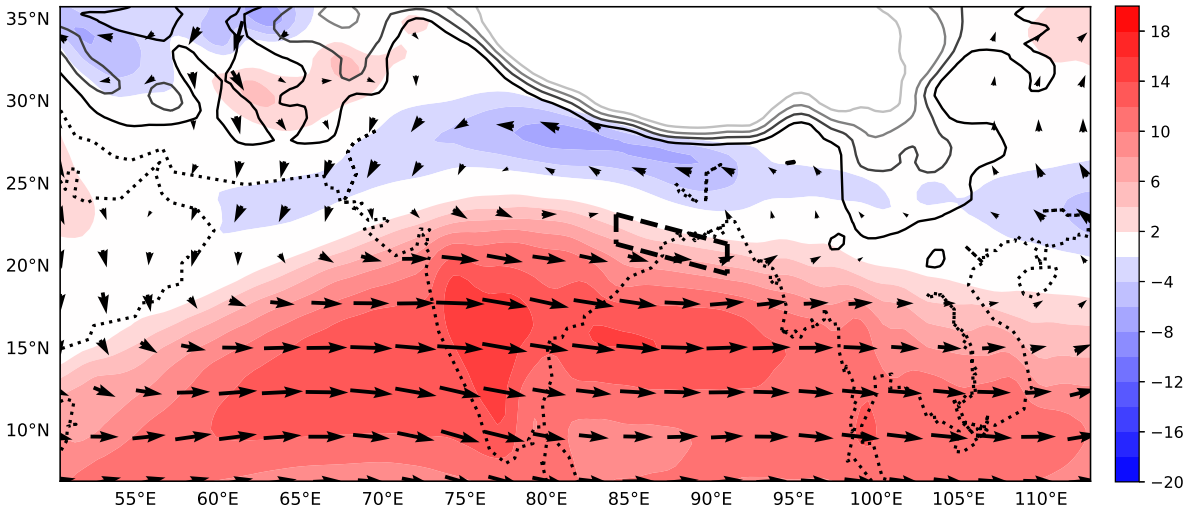

Figure 1. Basic state zonal wind ($\bar{U}$, shading, $\mathrm{m\,s^{-1}}$, 3.1 km), basic state wind ($\overline{\mathbf{V}}$, vectors, 3.1 km), and height of topography (contoured every 1.0 km). Dashed box shows the region where heating is applied in Exp. C.

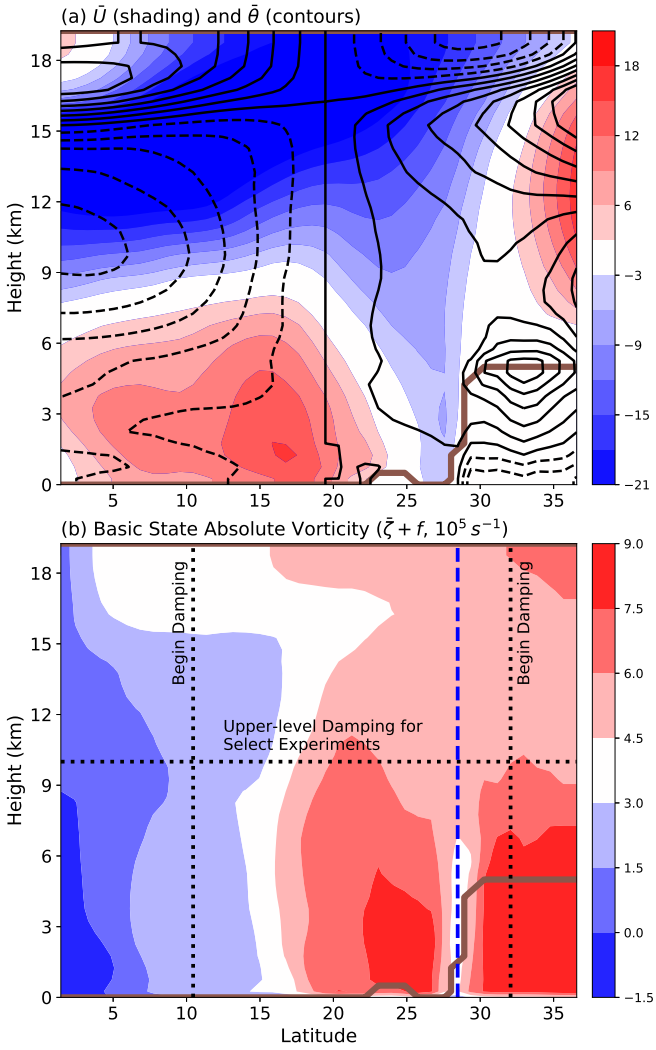

Figure 2. Latitude-height cross section at 87°E of the (a) basic state zonal winds ($\bar{U}$, shading, ms^{-1}) and basic state potential temperature ($\bar{\theta}$, contoured every 1.3 K with solid lines indicating positive values) and (b) basic state absolute vorticity ($\bar{\zeta}+f$, shading, s^{-1}). The topography is outlined in brown in both plots. The dotted black lines in (b) show the location of the boundary conditions used for some of the experiments in Exp. A. The dashed blue line shows the location north of which the basic state fields are set to a constant in Exp. A. Refer to Sec. 3.1 for further details.

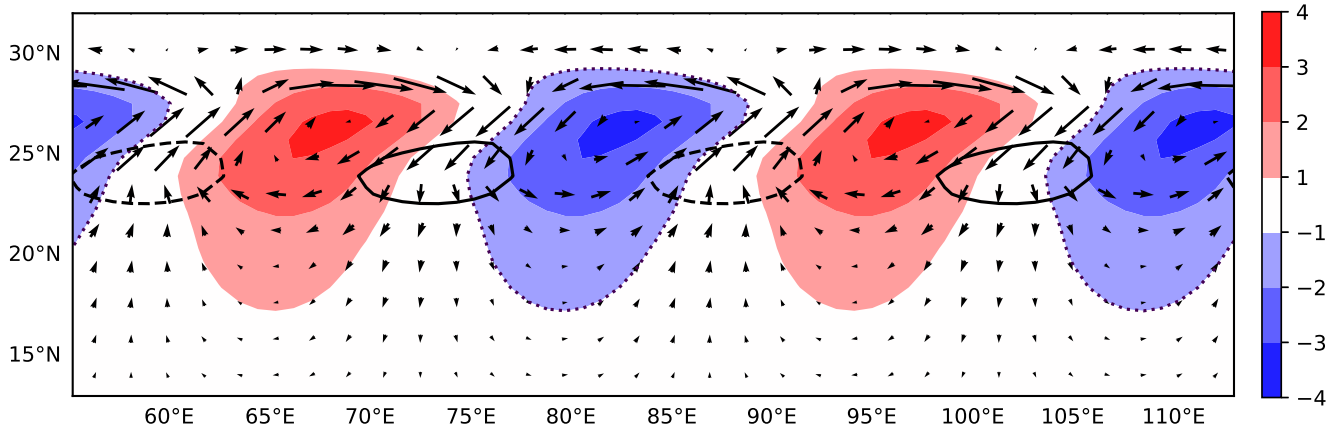

Figure 3. Perturbation pressure (p', shading, hPa, 3.25 km), perturbation winds ($\mathbf{v}'$, vectors, 3.25 km), and perturbation vertical velocity (w', contoured every $0.3\,\mathrm{cm\,s^{-1}}$, averaged from 1.0 km to 5.0 km) for the 3200 km wavelength normal mode from Exp. A. Negative values of p' are enclosed with a dotted line.

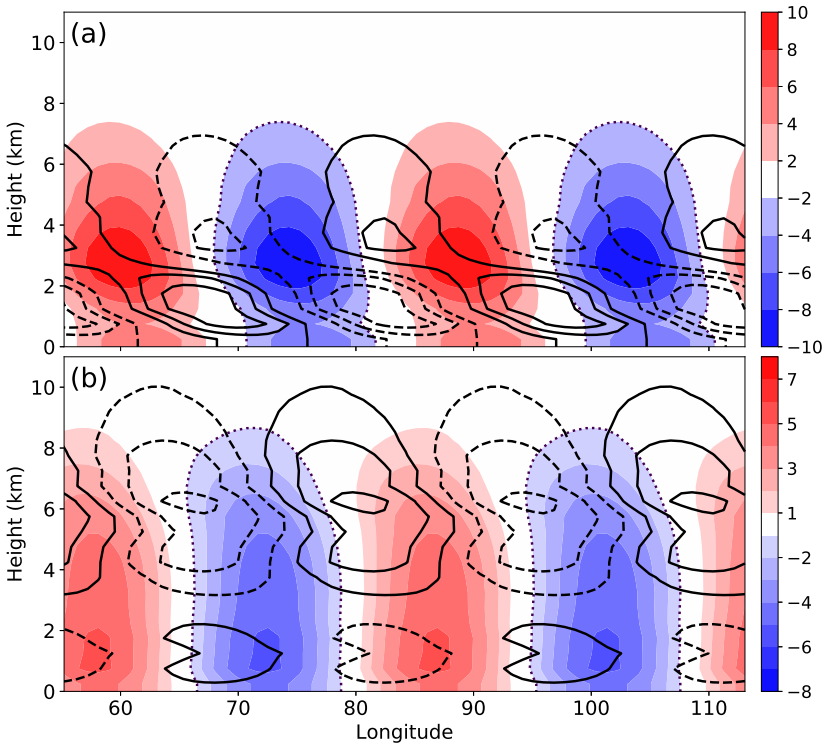

Figure 4. Longitude-height cross section for Exp. A at (a) 25.7°N and (b) 21.2°N of perturbation wind (v', shading, $\mathrm{m\,s^{-1}}$) and perturbation potential temperature (θ', contoured every 1.6 K for (a) and 0.63 K for (b), zero contour excluded) for the 3200 km wavelength normal mode. Negative values of v' are enclosed with a dotted line. Note the change in the shading scale for the wind.

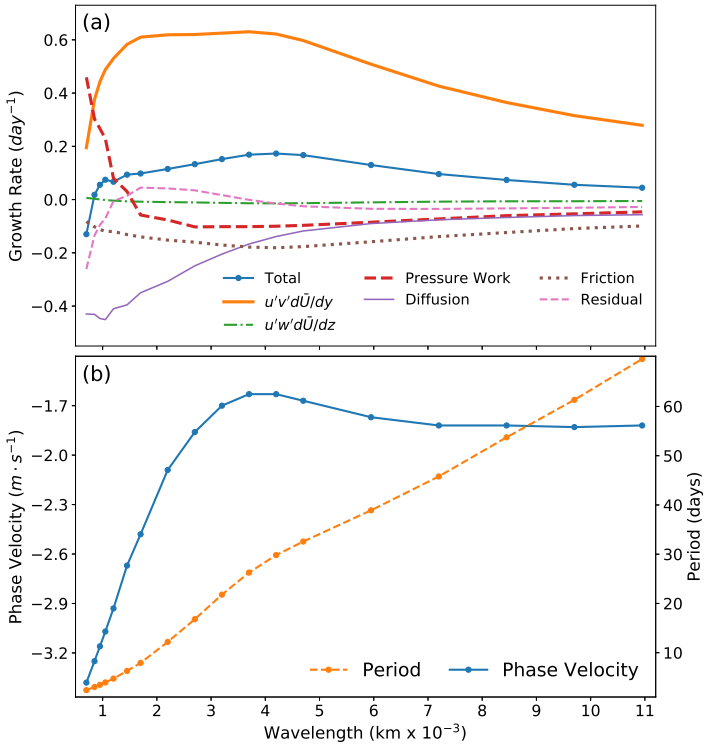

Figure 5. As a function of wavelength, (a) growth rates ($\mathrm{d^{-1}}$) for individual terms in Eq. 16 and (b) zonal phase velocity and period and for Exp. A. The individual experiments used to construct this relationship are marked by dots in the total growth rate for (a) and in both curves for (b).

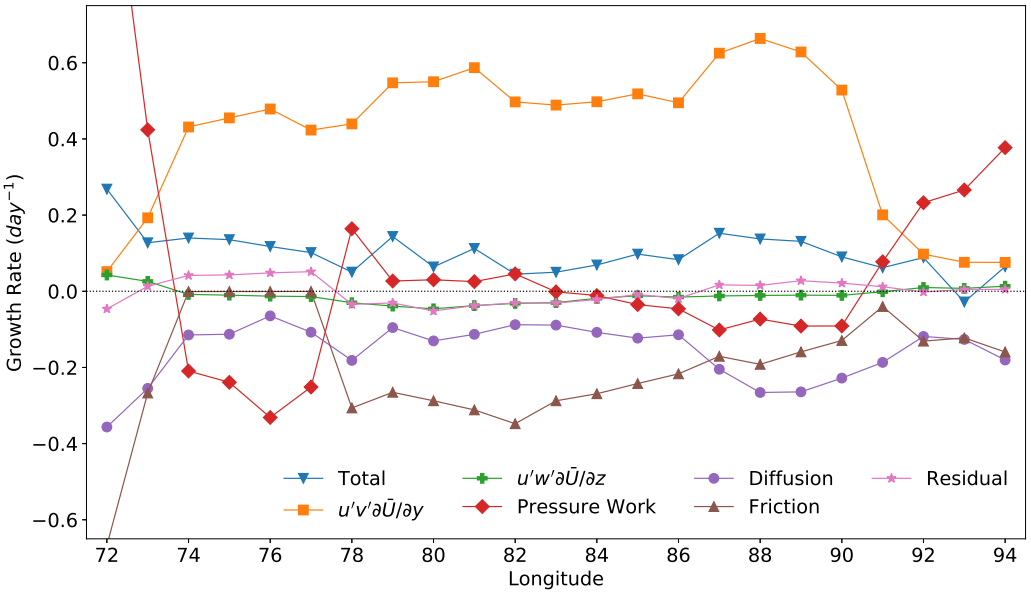

Figure 6. Growth rates as a function of longitude for indiviual terms in Eq. 16 for Exp. A. The individual experiments used to construct this relationship are marked by the various symbols. For presentation, the values for the 72°E pressure work ($1.24\,\mathrm{d}^{-1}$) and friction ($-0.67\,\mathrm{d}^{-1}$) terms are cut off.

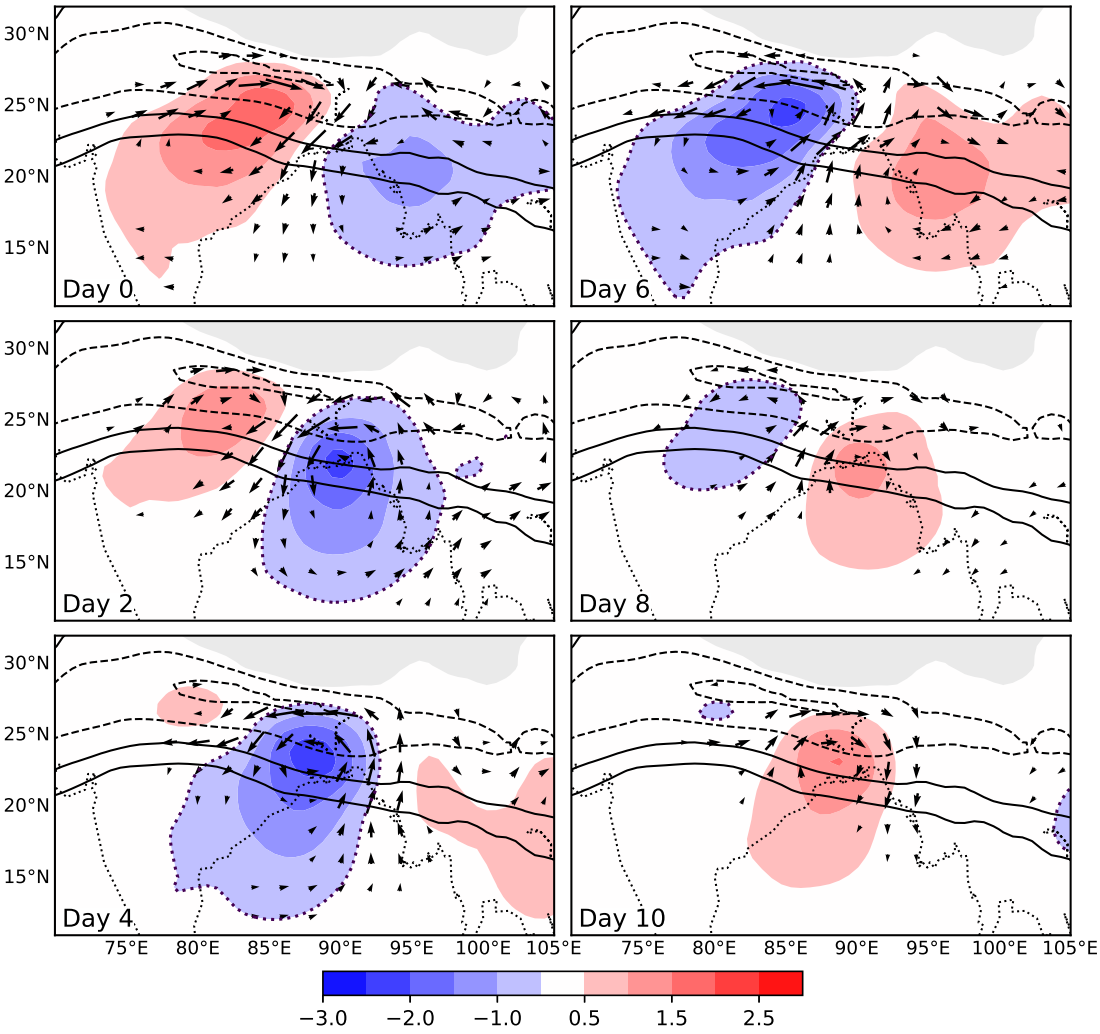

Figure 7. Time evolution of perturbation pressure (p', shading, hPa, 3.25 km), perturbation winds ($\mathbf{v}'$, vectors, 3.25 km), and basic state zonal wind ($\bar{U}$, contoured every $4\,\mathrm{m\,s}^{-1}$ between $-6\,\mathrm{m\,s}^{-1}$ and $6\,\mathrm{m\,s}^{-1}$, 3.25 km) for Exp. B. Negative values of p' are enclosed with a dotted line and regions below the terrain height are masked in gray.

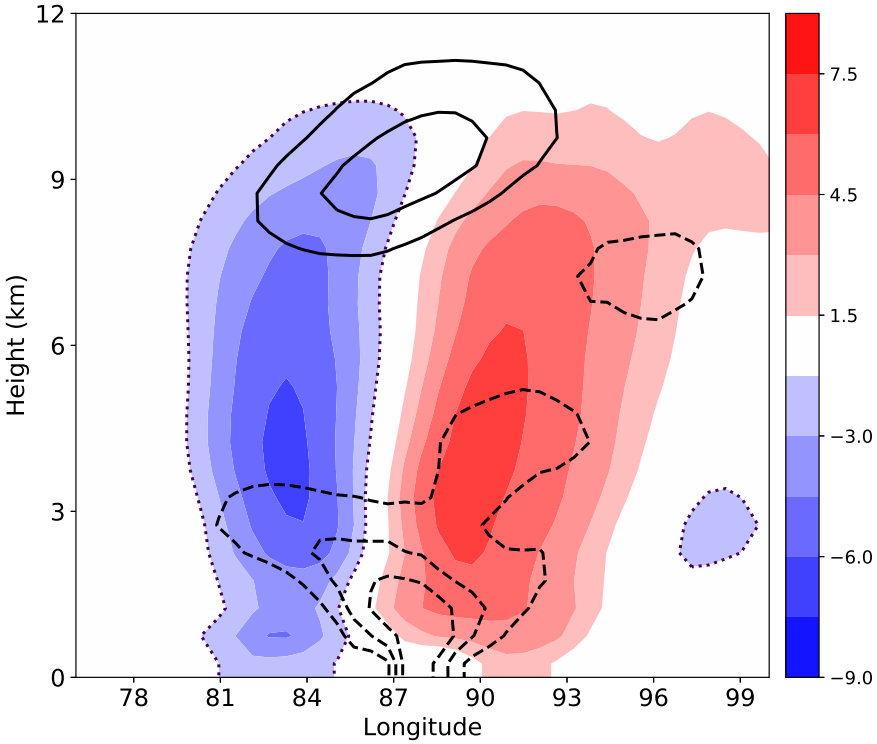

Figure 8. Longitude-height cross section of the component of perturbation wind orthogonal to the cross section (shading, $\mathrm{m\,s^{-1}}$) and perturbation potential temperature (θ', contoured every 1 K excluding zero contour) at day 5 for Exp. B. Negative values of v' are enclosed with a dotted line. This cross section is rotated 30° clockwise from a line of constant latitude and the fields are averaged for 225 km on either side of the cross section. Because of this rotation, longitude on the x-axis corresponds to 0.87 of its normal length.

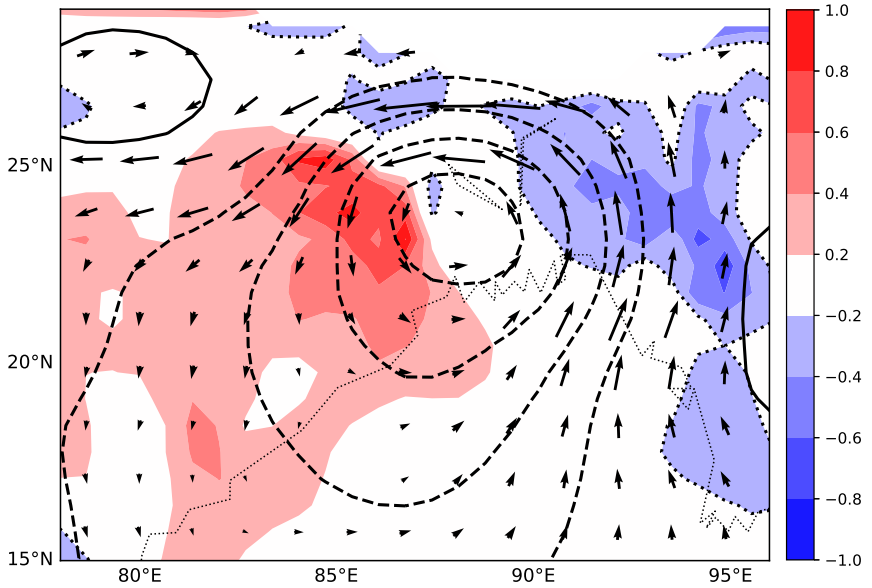

Figure 9. Perturbation vertical velocity (w', shading, $\mathrm{cm\,s^{-1}}$, averaged from 1.0 to 5.0 km) and perturbation winds ($\mathbf{v}'$, vectors, 3.25 km) at day 4 for Exp. B. Negative values of w' are enclosed with a dotted line.

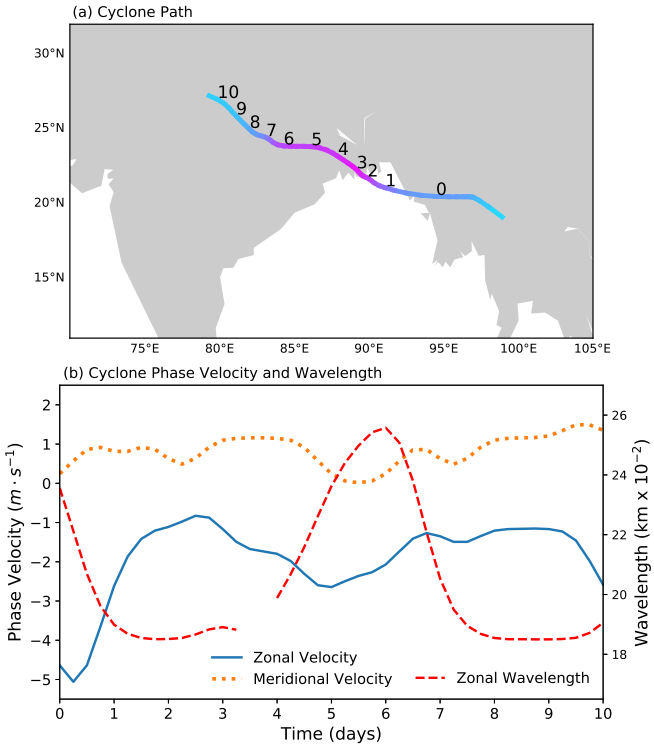

Figure 10. For Exp. B, (a) track of the center of the cyclonic phase of the wave disturbance shaded by magnitude of pressure perturbation and overlaid with dates corresponding to Fig. 7 and (b) zonal and meridional phase velocity and zonal wavelength as a function of time. For the pressure perturbation, lighter pinks correspond to lower pressure values and lighter blues to higher values.

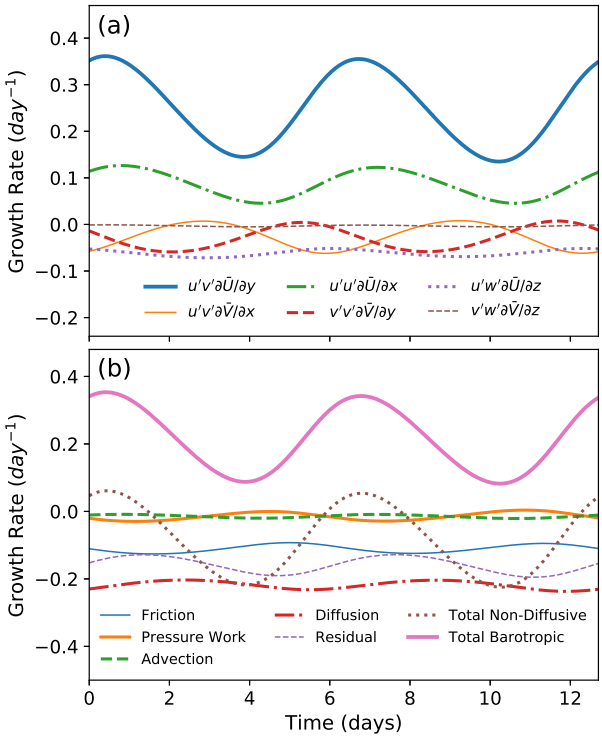

Figure 11. Growth rate (d^{-1}) as a function of time with dates corresponding to Fig. 7 for Exp. B. Panel (a) shows the barotropic terms from Eq. 16 and panel (b) shows the remaining terms in Eq. 16 along with the sum of the barotropic terms.

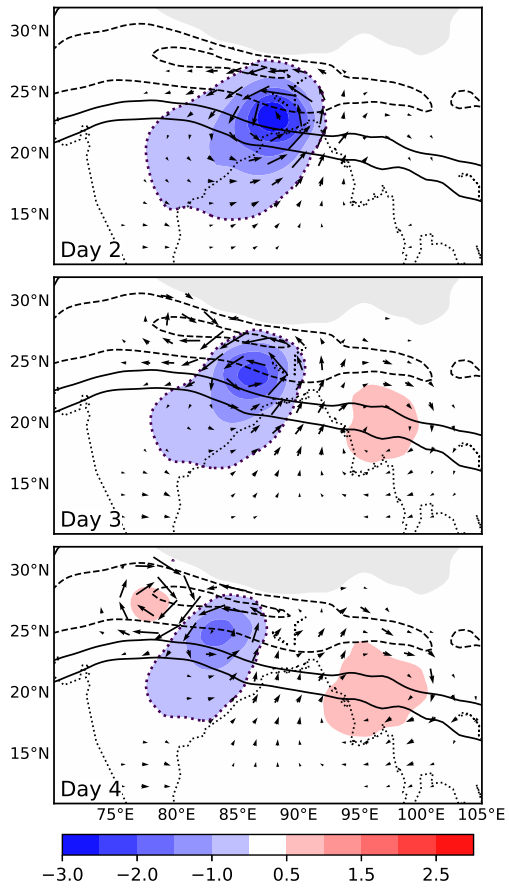

Figure 12. Perturbation pressure (p', shading, hPa, 3.1 km), perturbation winds ($\mathbf{v}'$, vectors, 3.1 km), and basic state zonal wind ($\bar{U}$, contoured every $4\,\mathrm{m\,s^{-1}}$ between $-6\,\mathrm{m\,s^{-1}}$ and $6\,\mathrm{m\,s^{-1}}$, 3.1 km) for Exp. C at 2, 3, and 4 days into the simulation with a basic state representative of the monsoon region. Negative values of p' are enclosed with a dotted line and regions below the terrain height are masked in gray.

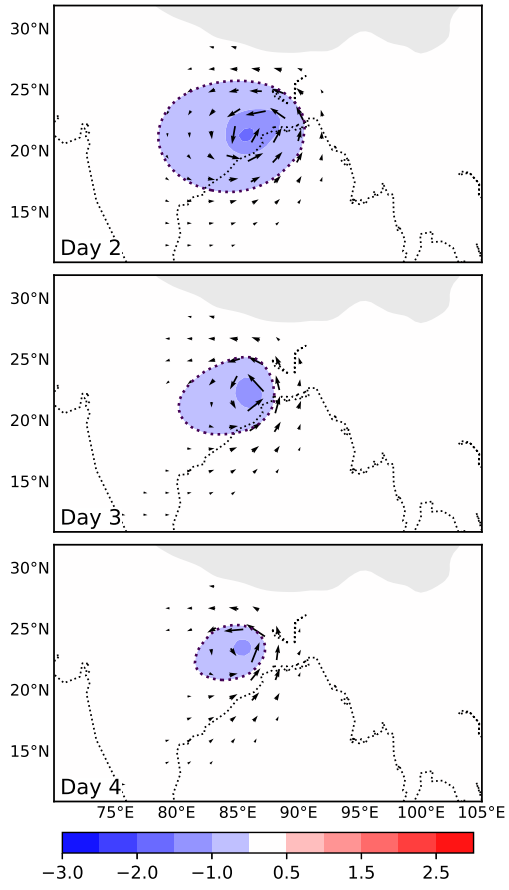

Figure 13. As in Fig. 12, but with the resting basic state.

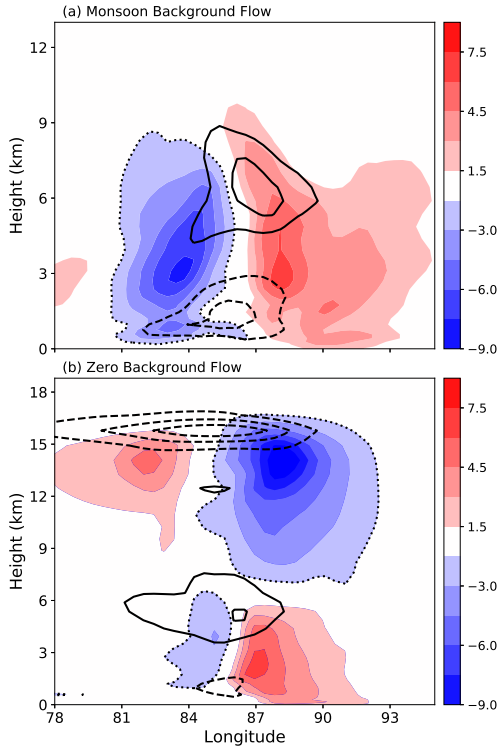

Figure 14. Longitude-height cross section of the component of perturbation wind orthogonal to cross section (shading, $\mathrm{m\,s^{-1}}$) and perturbation potential temperature (θ', K, contours) for Exp. C at 3 days into the simulation for (a) monsoon basic state and (b) resting basic state. Negative values of v' are enclosed with a dotted line. This cross section is rotated 30° clockwise from a line of constant latitude and the fields are averaged for 150 km on either side of the cross section. Because of this rotation, longitude on the x-axis corresponds to 0.87 of its normal length. Note the change in the y-axis scale.

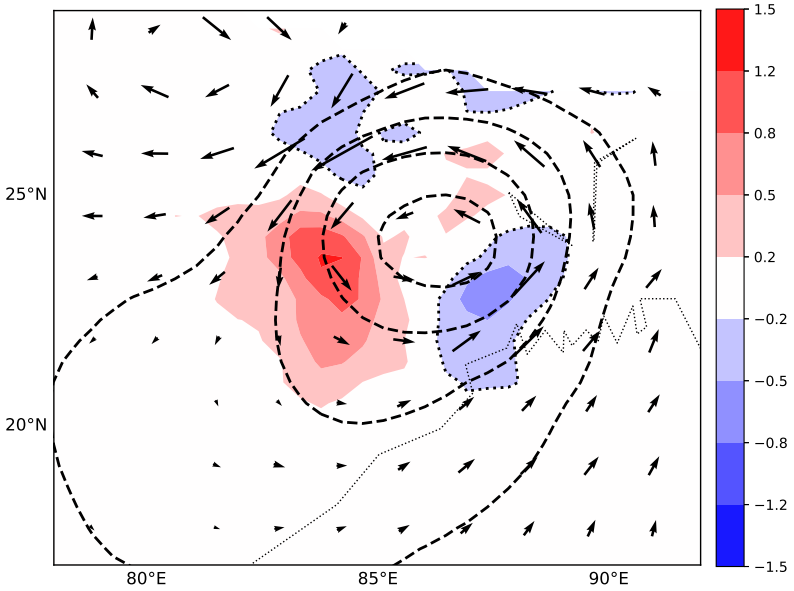

Figure 15. Perturbation vertical velocity (w', shading, $\mathrm{cm\,s^{-1}}$, averaged from 1.2 to 5.3 km) and perturbation winds ($\mathbf{v}'$, vectors, 3.1 km) for Exp. C at 72 hours into the simulation. Negative values of w' are enclosed with a dotted line.

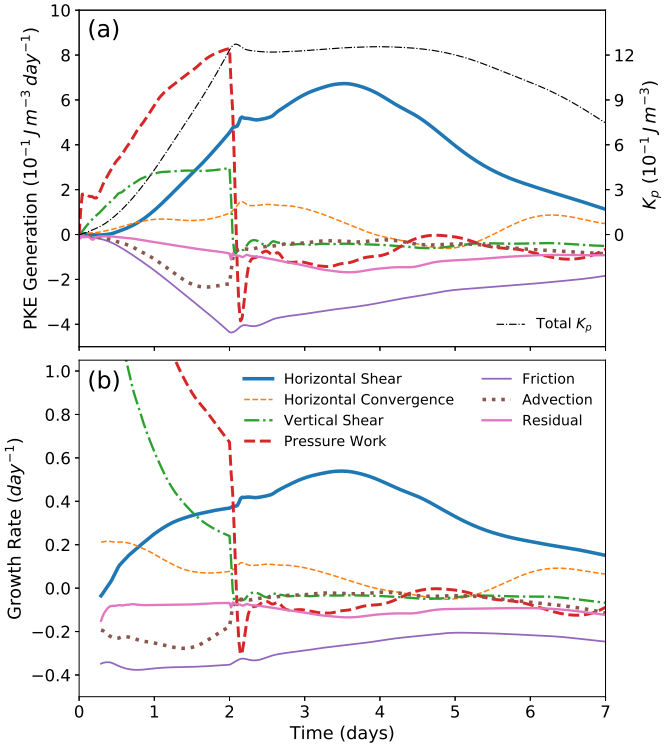

Figure 16. Terms in K_p budget (Eq. 16) for Exp. C using the monsoon basic state. Panel (a) shows K_p generation rates and total K_p and Panel (b) shows growth rates. The legend in (b) also applies to (a)

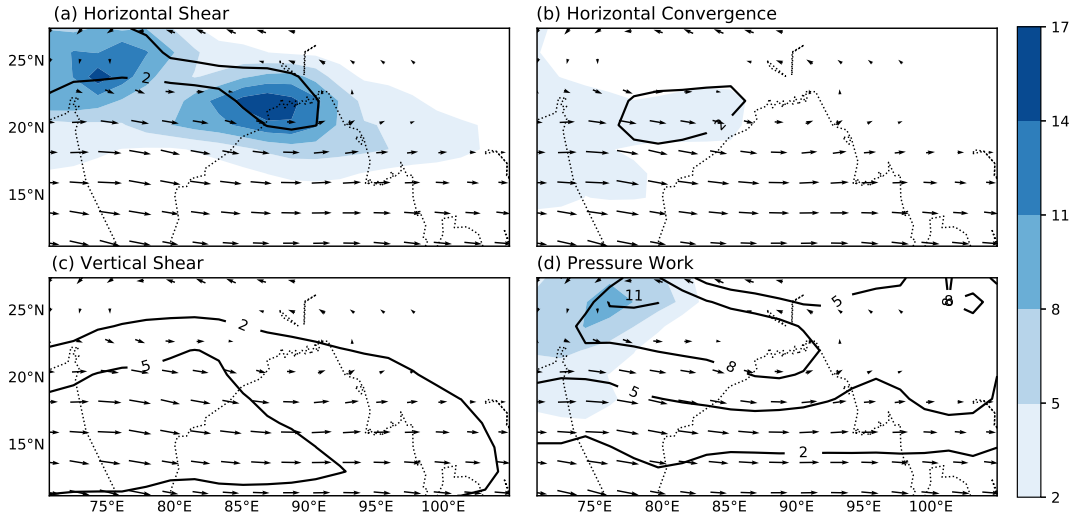

Figure 17. Total perturbation kinetic energy generated by select terms in Eq. 16 (shading, J m^{-3}) and basic state winds (vectors, 3.1 km). Contours show values integrated from 0 to 48 hours of each simulation and colors show values integrated from 51 to 144 hours. The numerical value for each of the 200 simulations is plotted at the center of the heating perturbation.

